

1 **Title: ESCRT recruitment to mRNA-encoded SARS-CoV-2 spike induces virus-
2 like particles and enhanced antibody responses**

3

4 **Authors:** Magnus A. G. Hoffmann^{1*}, Zhi Yang^{1‡}, Kathryn E. Huey-Tubman¹,
5 Alexander A. Cohen¹, Priyanthi N. P. Gnanapragasam¹, Leesa M. Nakatomi¹, Kaya
6 N. Storm¹, Woohyun J. Moon², Paulo J.C. Lin², Pamela J. Bjorkman^{1*}

7

8 **Affiliations:**

9 ¹Division of Biology and Biological Engineering, California Institute of Technology,
10 Pasadena, CA 91125, USA

11 ²Acuitas Therapeutics, Vancouver, BC, V6T 1Z3, CANADA

12 [‡]Present address: Department of Molecular and Cell Biology, University of California,
13 Berkeley, CA 94720, USA

14

15 *To whom correspondence should be addressed: Email: mhoffman@caltech.edu,
16 bjorkman@caltech.edu

17

18 **Summary**

19 Prime-boost regimens for COVID-19 vaccines elicit poor antibody responses against
20 Omicron-based variants and employ frequent boosters to maintain antibody levels.
21 We present a natural infection-mimicking technology that combines features of mRNA-
22 and protein nanoparticle-based vaccines through encoding self-assembling
23 enveloped virus-like particles (eVLPs). eVLP assembly is achieved by inserting an
24 ESCRT- and ALIX-binding region (EABR) into the SARS-CoV-2 spike cytoplasmic tail,
25 which recruits ESCRT proteins to induce eVLP budding from cells. Purified spike-
26 EABR eVLPs presented densely-arrayed spikes and elicited potent antibody
27 responses in mice. Two immunizations with mRNA-LNP encoding spike-EABR elicited
28 potent CD8+ T-cell responses and superior neutralizing antibody responses against
29 original and variant SARS-CoV-2 compared to conventional spike-encoding mRNA-
30 LNP and purified spike-EABR eVLPs, improving neutralizing titers >10-fold against
31 Omicron-based variants for three months post-boost. Thus, EABR technology
32 enhances potency and breadth of vaccine-induced responses through antigen
33 presentation on cell surfaces and eVLPs, enabling longer-lasting protection against
34 SARS-CoV-2 and other viruses.

35

36

37

38 **Introduction**

39 mRNA vaccines emerged during the COVID-19 pandemic as an ideal platform for the
40 rapid development of effective vaccines (Corbett et al., 2020). Currently approved
41 SARS-CoV-2 mRNA vaccines encode the viral spike (S) trimer (Zheng et al., 2022),
42 the primary target of neutralizing antibodies during natural infections (Chen et al.,
43 2022). Clinical studies have demonstrated that mRNA vaccines are highly effective,
44 preventing >90% of symptomatic and severe SARS-CoV-2 infections (Baden et al.,
45 2021; Polack et al., 2020) through both B and T cell responses (Kent et al., 2022).
46 mRNA vaccines in part mimic an infected cell since expression of S within cells that
47 take up S-encoding mRNAs formulated in lipid nanoparticles (LNP) (Hogan and Pardi,
48 2022) results in cell surface expression of S protein to stimulate B cell activation.
49 Translation of S protein inside the cell also provides viral peptides for presentation on
50 MHC class I molecules to cytotoxic T cells, which does not commonly occur in protein
51 nanoparticle-based vaccines (Rock et al., 2016) that resemble the virus by presenting
52 dense arrays of S protein; e.g., the Novavax NVX-CoV2373 vaccine (Heath et al.,
53 2021; Keech et al., 2020). However, comparisons to COVID-19 mRNA vaccines
54 showed that NVX-CoV2373 elicits comparable neutralizing antibody titers (Karbiener
55 et al., 2022; Zhang et al., 2022), the main immune correlate of vaccine-induced
56 protection (Barouch, 2022), suggesting that potent B cell activation can be achieved
57 through presentation of viral surface antigens on cell surfaces or virus-resembling
58 nanoparticles. Achieving higher antibody neutralization titers is desirable as antibody
59 levels contract substantially over a period of several months (Zhang et al., 2022), and
60 SARS-CoV-2 variants of concern (VOCs) that are less sensitive to antibodies elicited
61 by vaccines or natural infection have been emerging (Chen et al., 2021; Hachmann et
62 al., 2022; Wu et al., 2021). An optimal vaccine might therefore combine attributes of

63 both mRNA- and protein nanoparticle-based vaccines by delivering a genetically
64 encoded S protein that gets presented on cell surfaces and induces self-assembly and
65 release of S-presenting nanoparticles.

66

67 Here, we describe a novel technology that engineers membrane proteins to induce
68 self-assembly of enveloped virus-like particles (eVLPs) that bud from the cell surface.
69 This is accomplished for the SARS-CoV-2 S protein by inserting a short amino acid
70 sequence (termed an ESCRT- and ALIX-binding region or EABR) (Lee et al., 2008) at
71 the C-terminus of its cytoplasmic tail to recruit host proteins from the endosomal
72 sorting complex required for transport (ESCRT) pathway. Many enveloped viruses
73 recruit ESCRT-associated proteins such as TSG101 and/or ALIX through capsid or
74 other interior viral structural proteins during the budding process (McCullough et al.,
75 2018; Votteler and Sundquist, 2013). Thus, fusing the EABR to the cytoplasmic tail of
76 a viral glycoprotein or other membrane protein directly recruits TSG101 and ALIX,
77 bypassing the need for co-expression of other viral proteins for eVLP self-assembly.
78 Cryo-electron tomography (cryo-ET) showed dense coating of spikes on purified S-
79 EABR eVLPs, and direct injections of the eVLPs elicited potent neutralizing antibody
80 responses in mice. Finally, we demonstrate that an mRNA vaccine encoding the S-
81 EABR construct elicited at least 5-fold higher neutralizing antibody responses against
82 SARS-CoV-2 and VOCs in mice than a conventional S-encoding mRNA vaccine or
83 purified S-EABR eVLPs. These results demonstrate that mRNA-mediated delivery of
84 S-EABR eVLPs elicits superior antibody responses, suggesting that dual presentation
85 of viral surface antigens on cell surfaces and on extracellular eVLPs has the potential
86 to enhance the effectiveness of COVID-19 mRNA vaccines.

87

88 **Results**

89 **ESCRT recruitment to the spike cytoplasmic tail induces eVLP assembly**

90 To evaluate the hypothesis that direct recruitment of ESCRT proteins to the
91 cytoplasmic tail of a SARS-CoV-2 S protein could result in self-assembly and budding
92 of eVLPs, we fused EABRs derived from different sources to the truncated cytoplasmic
93 tail of the S protein, separated from its C-terminus by a short Gly-Ser linker (Figures
94 1A and 1B). The S protein contained the D614G substitution (Korber et al., 2020), a
95 furin cleavage site, two proline substitutions (2P) in the S2 subunit to stabilize the
96 prefusion conformation (Pallesen et al., 2017), and the C-terminal 21 residues were
97 truncated to optimize cell surface expression by removing an endoplasmic reticulum
98 (ER)-retention signal (Δ CT) (McBride et al., 2007) (Figure 1B). We evaluated the
99 EABR fragment from the human CEP55 protein that binds TSG101 and ALIX during
100 cytokinesis (Lee et al., 2008) (Figure 1B). For comparisons, viral late domains that
101 recruit early ESCRT proteins during the viral budding process were obtained from the
102 Equine Infectious Anemia Virus (EIAV) p9 protein (Fisher et al., 2007), residues 1-44
103 of the Ebola virus (EBOV) VP40 protein (Madara et al., 2015), and the HIV-1 p6 protein
104 (Fujii et al., 2009) (Figure S1A). We hypothesized that eVLP production could be
105 enhanced by preventing endocytosis of EABR-fusion proteins to extend the duration
106 that proteins remain at the plasma membrane to interact with ESCRT proteins. We
107 therefore added an endocytosis prevention motif (EPM), a 47-residue insertion derived
108 from the murine Fc gamma receptor FcgRBII-B1 cytoplasmic tail (Figures 1A and 1B)
109 that tethers FcgRBII-B1 to the cytoskeleton to prevent coated pit localization and
110 endocytosis (Miettinen et al., 1989).

111

112 The abilities of the S-EABR, S-p9, S-VP40₁₋₄₄, and S-p6 constructs to generate eVLPs
113 were evaluated by transfecting Expi293F cells and measuring eVLP production in
114 supernatants from which eVLPs were purified by ultracentrifugation on a 20% sucrose
115 cushion. Western blot analysis showed that the highest S protein levels were detected
116 for the S-EABR construct, suggesting that the CEP55 EABR induced efficient self-
117 assembly of S-containing eVLPs (Figures 1C and S1B). At a sample dilution of 1:400,
118 the S-EABR construct produced a similarly intense band compared to the S-p9
119 construct at a 1:40 dilution, suggesting that S protein levels were ~10-fold higher. The
120 CEP55 EABR binds both ALIX and TSG101 (Lee et al., 2008), whereas EIAV p9 only
121 binds ALIX (Fisher et al., 2007), suggesting that optimal recruitment of both ESCRT
122 proteins is required for efficient eVLP assembly. The S-p6 and S-VP40₁₋₄₄ samples
123 contained little or no S protein suggesting that eVLP assembly was inefficient, possibly
124 resulting from lower affinities for ESCRT proteins (Figures 1C and S1B).

125
126 We further characterized the S-EABR construct by experimenting with different EABR
127 sequences (Figure S1A), finding that addition of a second EABR domain (S-2xEABR)
128 reduced eVLP production (Figure 1D). To investigate whether S-EABR eVLP
129 assembly is dependent on ESCRT recruitment, we generated S-EABR_{mut} by
130 substituting an EABR residue (Tyr187 in CEP55) that is essential for interacting with
131 ALIX (Lee et al., 2008) (Figure S1A). While the purified S-EABR eVLP sample
132 produced an intense band at a 1:200 dilution, no band was detected for S-EABR_{mut} at
133 a 1:20 dilution, suggesting that eVLP production was abrogated for S-EABR_{mut} and
134 highlighting the importance of ALIX recruitment for eVLP assembly (Figure 1D). To
135 identify the minimal EABR sequence required for eVLP assembly, we designed S
136 constructs fused to the complete EABR domain (CEP55₁₇₀₋₂₁₃), EABR_{min1} (CEP55₁₈₀₋

137 213), and EABR_{min2} (CEP55₁₈₀₋₂₀₄) (Figure S1a). While S-EABR eVLP yields were
138 diminished for EABR_{min2}, production efficiency was retained for EABR_{min1} (Figure 1E).
139 To assess the effects of the EPM within the cytoplasmic tail of the S-EABR construct,
140 we evaluated eVLP production for an S-EABR construct that did not include the EPM.
141 Western blot analysis demonstrated that increased amounts of S protein were
142 detected after eVLP purification from cells transfected with S-EABR compared to S-
143 EABR/no EPM, suggesting that the EPM enhances eVLP production (Figure 1F).

144

145 We also compared the S-EABR construct to other eVLP approaches (Martins et al.,
146 2022) that require co-expression of S protein with structural viral proteins, such as
147 HIV-1 Gag (Hoffmann et al., 2020) or the SARS-CoV-2 M, N, and E proteins (Syed et
148 al., 2021). Western blot analysis showed that purified S-EABR eVLP fractions
149 contained at least 10-fold more S protein than eVLPs produced by co-expression of S
150 and Gag or S, M, N, and E (Figure 1G), suggesting that S-EABR eVLPs assemble
151 and/or incorporate S proteins more efficiently than the other eVLP approaches.
152 Purified S-EABR eVLPs also contained higher levels of S protein compared to S-
153 ferritin nanoparticles purified from transfected cell supernatants, which have been
154 shown to elicit potent immune responses in animal models (Joyce et al., 2021; Powell
155 et al., 2021) (Figure 1G).

156

157 3D reconstructions derived from cryo-ET showed purified S-EABR eVLPs with
158 diameters ranging from 40 - 60 nm that are surrounded by a lipid bilayer and the
159 majority of which were densely coated with spikes (Figures 1H and 1I; Movie S1). To
160 estimate the number of S trimers, we counted trimer densities in ~4 nm computational
161 tomographic slices of individual eVLPs, finding ~10-40 spikes per particle that were

162 heterogeneously distributed on the surface of eVLPs. The upper limit of the number of
163 spikes on eVLPs roughly corresponds to spike numbers on larger SARS-CoV-2 virions
164 (>100 nm in diameter) (Ke et al., 2020); thus, the spike densities on the majority of
165 eVLPs exceed those on authentic viruses. Spikes on eVLPs were separated by
166 distances of ~20-26 nm (measured between the centers of trimer apexes) for densely
167 coated particles (Figures 1H and 1I). To assess the general applicability of the EABR
168 approach, we also generated EABR eVLPs for HIV-1 Env, which produced eVLPs with
169 higher Env content than co-expression of Env and HIV-1 Gag (Figure S1C), and for
170 the multi-pass transmembrane protein CCR5 (Figure S1D). Taken together, these
171 results are consistent with efficient incorporation of S proteins into S-EABR eVLPs that
172 are released from transfected cells and suggest that the EABR technology can be
173 applied to a wide range of membrane proteins.

174

175 **S-EABR eVLPs induce potent antibody responses in immunized mice**

176 The potential of purified S-EABR eVLPs as a vaccine candidate against SARS-CoV-
177 2 was evaluated in C57BL/6 mice (Figure 2A). S-EABR eVLPs were purified from
178 transfected cell supernatants by ultracentrifugation on a 20% sucrose cushion
179 followed by size exclusion chromatography (SEC), and S protein concentrations were
180 determined by quantitative Western blot analysis (Figures S2A and S2B). For a 100
181 mL transfection of Expi293F cells, purified S-EABR eVLPs from supernatants
182 contained ~250-500 µg S protein. Immunizations with S-EABR eVLPs were compared
183 to purified soluble S and to soluble S covalently attached to SpyCatcher-mi3 protein
184 nanoparticles (S-mi3) (Keeble et al., 2019). 0.1 µg doses (calculated based on S
185 protein content) were administered by subcutaneous injections on days 0 and 28 for
186 all immunogens in the presence of Sigma adjuvant (Figure 2A), and we evaluated

187 serum antibody responses by enzyme-linked immunosorbent assays (ELISAs) and in
188 vitro pseudovirus neutralization assays. After the prime, S-EABR eVLPs elicited robust
189 antibody binding and neutralization responses in all mice against SARS-CoV-2 (WA1
190 variant including the D614G substitution (WA1/D614G)), similar to titers elicited by S-
191 mi3 (Figures 2B and 2C). In contrast, no neutralizing antibody responses were
192 detected for soluble S protein immunization after the prime. Neutralizing antibody titers
193 elicited by S-EABR eVLPs and S-mi3 increased by >10-fold after boosting and were
194 >20-fold higher than titers measured for soluble S (Figure 2C). S-EABR eVLPs elicited
195 potent antibody responses targeting the receptor-binding domain (RBD) of the S
196 protein (Figure S2C), a primary target of anti-SARS-CoV-2 neutralizing antibodies
197 (Kleanthous et al., 2021). Serum responses were also evaluated against authentic
198 SARS-CoV-2 by plaque reduction neutralization tests (PRNTs), showing robust
199 neutralizing activity against SARS-CoV-2 WA1 (Figure S2D). Neutralization titers
200 dropped ~4-fold and ~2-fold against the SARS-CoV-2 Beta and Delta variants,
201 respectively, consistent with studies of licensed vaccines that encode the SARS-CoV-
202 2 WA1 S protein (van Gils et al., 2022). These results demonstrate that purified S-
203 EABR eVLPs elicit potent immune responses in vivo and represent an alternative
204 technology for producing nanoparticle-based vaccines that does not involve detergent-
205 mediated cell lysis and separation of membrane protein antigens from cell lysates, as
206 required for protein nanoparticle vaccines such as NVX-CoV2373, a COVID-19
207 vaccine (Heath et al., 2021; Keech et al., 2020), or FluBlok, an influenza vaccine (Cox
208 and Hollister, 2009).

209

210

211 **mRNA-encoded S-EABR construct induces cell surface expression and eVLP
212 budding**

213 A key advantage of the EABR eVLP technology over existing nanoparticle-based
214 vaccine approaches is that S-EABR constructs can be easily delivered as mRNA
215 vaccines since both eVLP assembly and cell surface expression only require
216 expression of a single genetically encoded component. While conventional COVID-19
217 mRNA vaccines induce antibody responses through cell surface expression of S
218 protein (Figure 3A, top), mRNA-mediated delivery of an S-EABR construct could
219 enhance B cell activation because S-EABR proteins will not only be expressed at the
220 cell surface – they will also induce assembly of eVLPs that bud from the cell and
221 distribute inside the body to activate immune cells (Figure 3A, bottom).

222
223 To investigate whether genetic encoding of S-EABR eVLPs enhances the potency of
224 a SARS-CoV-2 S-based mRNA vaccine, we started by synthesizing nucleoside-
225 modified mRNAs encoding S, S-EABR, S-EPM, or S-EABR/no EPM. Cell surface
226 expression and eVLP assembly were evaluated by flow cytometry and Western blot
227 analysis 48 hours after in vitro transfection of mRNAs in HEK293T cells, demonstrating
228 higher surface expression for S compared to the S-EABR fusion protein (Figure 3B).
229 While addition of the EPM had little effect on S surface expression, removal of the
230 EPM lowered surface levels for the S-EABR construct. Western blot analysis of
231 supernatants confirmed that the S and S-EPM transfactions did not generate
232 detectable eVLPs in supernatants, whereas eVLPs were strongly detected in
233 supernatants from S-EABR transfected cells (Figure 3C). eVLP production was
234 decreased for S-EABR/no EPM, which together with the flow cytometry results (Figure

235 3B), suggests that EPM addition enhances both S-EABR cell surface expression and
236 eVLP assembly.

237

238 The observed reduction in S cell surface expression in the S-EABR versus S mRNA
239 transfections could be caused by lower overall cell surface expression of the S-EABR
240 fusion protein, incorporation of S-EABR proteins into eVLPs that bud from the cell
241 surface, or both. To evaluate these possibilities, we calculated approximate numbers
242 of S trimers expressed from the S-EABR construct. Assuming that 3×10^6 cells were
243 transfected (6-well plate) and up to 1×10^5 S trimers were expressed on the surface of
244 each cell (based on the approximate number of B cell receptors on a B cell (Alberts et
245 al., 2002)), transfected cell surfaces would contain ~ 0.5 pmol or ~ 70 ng of total S
246 protein. Supernatant samples for Western blots were concentrated to a final volume
247 of 200 μ L of which 1.2 μ L was loaded onto a gel. As the detection limit for S1 is ~ 20
248 ng, the Western blot analysis suggested that purified S-EABR eVLPs from transfected
249 cell supernatants contained at least ~ 17 ng/ μ L S protein, corresponding to >3 μ g S
250 protein in the purified transfected cell supernatant. These calculations suggested that
251 the observed reduction in cell surface expression for the S-EABR construct was at
252 least partially caused by incorporation of S-EABR proteins into budding eVLPs that
253 were released into the supernatant. Given that the estimated S protein content on
254 released eVLPs exceeded the approximate amount of S protein presented on cell
255 surfaces, it is possible that the S-EABR construct induces higher overall expression of
256 S antigens compared to S for which expression is restricted to cell surfaces. Taken
257 together, the mRNA transfection results demonstrate that the mRNA-encoded S-
258 EABR construct enables dual presentation of S antigens on cell surfaces and released
259 eVLPs.

260 **S-EABR mRNA-LNP elicit superior antibody titers compared to conventional
261 vaccines**

262 The effect of eVLP production on mRNA vaccine potency was evaluated in BALB/c
263 mice by comparing mRNAs encoding S or S-EABR constructs that were encapsulated
264 in LNP (Figure 4A). As described for preclinical studies of a COVID-19 mRNA vaccine
265 in mice (Corbett et al., 2020), mRNA-LNP were administered intramuscularly (IM) at a
266 dose of 2 µg mRNA on days 0 and 28. mRNA-LNP immunizations were also compared
267 to purified S-EABR eVLPs that were injected IM in the presence of Addavax adjuvant.
268 Antibody binding and neutralizing responses were evaluated by ELISAs and
269 pseudovirus neutralization assays, respectively (Figures 4B-4H). After the prime, S
270 and S-EABR mRNA-LNP elicited significantly higher antibody binding responses
271 against the SARS-CoV-2 S protein than purified S-EABR eVLPs (Figure 4C).
272 However, the highest neutralizing antibody titers were elicited by purified S-EABR
273 eVLPs, which were significantly higher than titers elicited by the S mRNA-LNP (Figure
274 4D).

275
276 After a boost immunization, S-EABR mRNA-LNP elicited significantly higher binding
277 and neutralizing antibody titers than purified S-EABR eVLPs and S mRNA-LNP
278 (Figures 4B-4D). Geometric mean neutralization titers measured for S-EABR mRNA-
279 LNP were 5.1- and 5-fold higher than titers elicited by purified S-EABR eVLPs and S
280 mRNA-LNP, respectively (Figures 4B and 4D). Three months post-boost (day 112),
281 mean neutralization titers were 5.9- and 6.8-fold higher for S-EABR mRNA-LNP
282 compared to purified S-EABR eVLPs and S mRNA-LNP, respectively, demonstrating
283 that the increased serum neutralization activity was maintained (Figures 4B and 4D).

284

285 We also evaluated serum neutralizing activity against SARS-CoV-2 VOCs. S-EABR
286 mRNA-LNP elicited 4.9- and 6.5-fold higher mean neutralizing responses against the
287 Delta variant compared to S mRNA-LNP, as well as 4.6- and 9.4-fold higher titers
288 compared to purified S-EABR eVLPs on days 56 and 112, respectively (Figures 4B
289 and 4E). Against Omicron BA.1, neutralizing antibody responses dropped markedly
290 for all groups, except for mice that received S-EABR mRNA-LNP, which elicited 15.1-
291 and 9.5-fold higher neutralizing titers than S mRNA-LNP and 20.7- and 15.4-fold
292 higher titers than purified S-EABR eVLPs on days 56 and 112, respectively (Figures
293 4B and 4F). Against Omicron BA.2, mean neutralization titers measured for mice that
294 received S-EABR mRNA-LNP were also 10.9- and 8.2-fold higher compared to S
295 mRNA-LNP and 7- and 12.2-fold higher compared to purified S-EABR eVLPs on days
296 56 and 112, respectively (Figures 4B and 4G). Compared to BA.2 titers, neutralizing
297 antibody responses against the BA.4/5 variant decreased 4-8-fold for mice that
298 received S-EABR mRNA-LNP, but titers were still 3.4- and 4-fold higher (but not
299 statistically significant) compared to S mRNA-LNP and 4.2- and 6.8-fold higher
300 compared to purified S-EABR eVLPs on days 56 and 112, respectively (Figures 4B
301 and 4H). While neutralization titers of >1:400 against the BA.4/5 variant were
302 measured for 7 of 10 mice that received S-EABR mRNA-LNP on day 56, such
303 responses were only detected in 1 or 2 mice that received purified S-EABR eVLPs or
304 S mRNA-LNP, respectively. Together, these results demonstrate that mRNA-
305 mediated delivery of S-EABR eVLPs enhances the potency and breadth of humoral
306 immune responses in mice compared to conventional mRNA and protein nanoparticle-
307 based vaccine approaches. The observed improvements in neutralizing activity
308 against Omicron-based VOCs were substantially larger than the 1.5-fold increases
309 reported for recently approved bivalent mRNA booster shots (Khoury et al., 2022),

310 suggesting that S-EABR mRNA-LNP-based booster immunizations could induce more
311 effective and lasting immunity against Omicron-based and emerging VOCs than
312 current COVID-19 vaccines.

313

314 **S-EABR mRNA-LNP induce potent T cell responses**

315 On day 112 (3 months post-boost), splenocytes were isolated from immunized mice
316 to analyze T cell responses by enzyme-linked immunosorbent spot (ELISpot) assays
317 (Ranieri et al., 2014). Splenocytes were stimulated with a pool of SARS-CoV-2 S-
318 specific peptides, and INF- γ and IL-4 secretion were measured to evaluate T cell
319 activation. mRNA-LNP encoding S and S-EABR constructs induced potent INF- γ
320 responses, consistent with the presence of S-specific cytotoxic CD8+ T cells and T
321 helper 1 ($T_{H}1$) cellular immune responses (Figure 5A). In contrast, INF- γ responses
322 were almost undetectable for mice immunized with purified S-EABR eVLPs (Figure
323 5A). These results were expected as mRNA-LNP immunizations result in intracellular
324 expression of S or S-EABR immunogens and MHC class I presentation of antigenic
325 peptides that activate CD8+ T cells, which does not commonly occur for protein
326 nanoparticle-based vaccines (Rock et al., 2016).

327

328 S-EABR mRNA-LNP induced significantly stronger IL-4 responses compared to S
329 mRNA-LNP and purified S-EABR eVLPs (Figure 5B), consistent with potent $T_{H}2$
330 cellular immune responses. While $T_{H}1$ - and $T_{H}2$ -biased responses were observed for
331 S mRNA-LNP and purified S-EABR eVLPs, respectively, S-EABR mRNA-LNP
332 induced a balanced $T_{H}1/T_{H}2$ response, thereby potently stimulating cellular and
333 humoral immune responses. Thus, S-EABR mRNA-LNP retain the ability of
334 conventional S mRNA-LNP to activate potent cytotoxic CD8+ T cell responses, while

335 also potently activating T_H2 CD4+ T cell responses to enhance humoral immune
336 responses leading to increased antibody potency and breadth.

337

338 **Discussion**

339 Here, we present a novel technology to generate eVLPs for vaccine and other
340 applications. The approach harnesses the ESCRT pathway that is involved in cell
341 division and viral budding (McCullough et al., 2018; Votteler and Sundquist, 2013) to
342 drive assembly and release of eVLPs that present membrane proteins containing a
343 cytoplasmic ESCRT-recruiting motif, the EABR sequence from the human
344 centrosomal protein CEP55 (van der Horst et al., 2009). Our results demonstrate that
345 the EABR-based platform produces eVLPs that incorporate higher levels of membrane
346 antigens compared to approaches that require co-expression of the antigen with viral
347 capsid proteins such as Gag or with the SARS-CoV-2 M, N, and E proteins. Purified
348 S-EABR eVLPs elicited potent antibody responses against SARS-CoV-2 in mice that
349 were similar in magnitude to those elicited by a 60-mer protein nanoparticle displaying
350 S trimers. Compared to existing protein nanoparticle-based vaccine approaches, the
351 EABR technology exhibits attractive manufacturing properties as (i) eVLP production
352 requires expression of only a single component, (ii) transmembrane proteins are
353 retained in their native membrane-associated conformation to ensure optimal protein
354 expression and stability, and (iii) fully assembled eVLPs can be purified directly from
355 culture supernatants without requiring detergent-mediated cell lysis and separation of
356 membrane protein antigens from cell lysates. The lipid bilayer surrounding eVLPs also
357 prevents off-target antibody responses against a nanoparticle scaffold that have been
358 reported for protein nanoparticle-based immunogens (Kraft et al., 2022). Due to its
359 modularity, flexibility, and versatility, the EABR technology could potentially be used

360 to generate eVLPs presenting a wide range of surface proteins for vaccine and
361 therapeutic applications.

362

363 To optimize the EABR technology, we evaluated several ESCRT-recruiting motifs for
364 their ability to drive eVLP assembly, including viral late domains from EIAV, HIV-1,
365 and EBOV. The EABR from CEP55 generated eVLPs 10-fold more efficiently than the
366 EIAV late domain p9. The EABR binds to ESCRT proteins ALIX and TSG101 (Lee et
367 al., 2008), while p9 binds only to ALIX (Fisher et al., 2007), suggesting that efficient
368 eVLP assembly requires recruitment of both proteins. HIV-1 p6 contains motifs that
369 interact with both TSG101 and ALIX (Fisher et al., 2007; Fujii et al., 2009), but S-p6
370 constructs did not induce detectable eVLP budding in our experiments, perhaps
371 because reported affinities are relatively low (Fisher et al., 2007; Pornillos et al., 2002)
372 compared to TSG101 and ALIX affinities reported for the EABR (Lee et al., 2008).
373 eVLP production might be optimized by designing ESCRT-binding motifs with
374 increased affinities for ESCRT proteins. We were able to enhance eVLP production
375 by including an EPM derived from the FcgRII-B1 cytoplasmic tail (Miettinen et al.,
376 1992) to reduce endocytosis of EABR-fusion proteins, which increased S-EABR cell
377 surface expression and eVLP production.

378

379 An advantage of the EABR technology is that constructs can be easily delivered as
380 mRNA vaccines since eVLP assembly requires expression of only a single
381 component. This strategy results in presentation of viral surface antigens on the cell
382 surface and on released eVLPs that could distribute throughout the body, thereby
383 combining immune responses elicited by both conventional mRNA and protein
384 nanoparticle-based vaccines. S-EABR mRNA-LNP elicited significantly higher binding

385 and neutralizing antibody responses compared to conventional S-based mRNA-LNP
386 analogous to current COVID-19 mRNA vaccines and to purified S-EABR eVLPs,
387 suggesting that dual presentation of viral surface antigens on cell surfaces and eVLPs
388 potentiates B cell activation. Presentation of viral surface antigens on cell surfaces
389 alone potentially restricts expression for conventional mRNA vaccines due to a finite,
390 and presumably limited, environment for insertion of both delivered and endogenous
391 membrane proteins. Thus, combining cell surface expression and eVLP release for
392 the S-EABR mRNA-LNP may increase overall presentation of viral surface antigens
393 to the immune system. It is also possible that mRNA-mediated S-EABR eVLP
394 production expands the biodistribution of viral surface antigens to more effectively
395 engage B cells in lymph nodes distant from the injection site. The enhanced humoral
396 immune responses elicited by S-EABR mRNA-LNP were consistent with potent T_H2
397 cellular responses observed in S-EABR mRNA-LNP-immunized mice, which were
398 more pronounced than in mice immunized with S mRNA-LNP or purified S-EABR
399 eVLPs. Importantly, cytotoxic CD8+ T cell responses were maintained in S-EABR
400 mRNA-LNP- compared to S mRNA-LNP-immunized animals. Thus, S-EABR mRNA-
401 LNP potently stimulate both cellular and humoral immune responses.

402

403 The higher peak antibody levels elicited by the S-EABR mRNA-LNP would likely
404 impact the durability of protective antibody responses. Notably, differences in serum
405 antibody titers across different immunizations were maintained until three months
406 post-boost, suggesting that antibody levels might contract at similar rates for the tested
407 vaccine types. Hence, the elevated peak antibody titers elicited by the S-EABR mRNA-
408 LNP could result in markedly prolonged periods of immune protection compared to
409 conventional vaccine approaches, which could minimize the need for frequent booster

410 immunizations. Long-term studies that monitor antibody levels for several months are
411 needed to elucidate the relationship between peak antibody titers and durability of
412 responses.

413

414 Two immunizations with S-EABR mRNA-LNP also elicited potent neutralizing antibody
415 responses against SARS-CoV-2 Delta and Omicron-based VOCs, suggesting that
416 higher antibody responses could lead to enhanced protection against viral escape
417 variants. The conventional S-based mRNA-LNP immunization only elicited weak
418 responses against Omicron-based VOCs, consistent with outcomes reported in
419 humans in which weak Omicron-specific responses to WA1-based vaccines were
420 enhanced after a 3rd immunization (Barouch, 2022; Gruell et al., 2022). S-EABR
421 mRNA-LNP elicited >10-fold higher neutralizing antibody titers against Omicron BA.1
422 and BA.2 VOCs compared to S mRNA-LNP after only two immunizations, suggesting
423 that the simple addition of a short EABR-encoding sequence to the spike gene in
424 current mRNA vaccines could have limited the global spread of Omicron-based VOCs.
425 Our results also suggest that S-EABR mRNA-LNP-based booster immunizations
426 would induce superior immunity against Omicron-based and emerging VOCs
427 compared with current boosting strategies, as bivalent booster shots that contain
428 ancestral and Omicron-based variants improve neutralizing antibody titers by only 1.5-
429 fold compared to conventional booster shots (Khoury et al., 2022). Future studies need
430 to investigate whether the observed increase in neutralization activity against
431 Omicron-based VOCs results from higher overall antibody levels and/or increased
432 antibody targeting of sub-immunodominant conserved epitopes on S trimer.

433

434 Enhanced antibody responses compared to S mRNA-LNP have also been reported
435 for co-delivery of mRNAs encoding SARS-CoV-2 S, M, and E proteins, which should
436 result in dual presentation of S on cell surfaces and released eVLPs (Lu et al., 2020).
437 However, higher mRNA doses (10 µg) were needed to deliver all three mRNAs, and
438 only modest improvements (~2.5-fold) in neutralizing antibody titers were achieved.
439 Our results showed that S-EABR eVLPs assemble more efficiently in vitro than eVLPs
440 driven by co-expression of S, M, N, and E proteins, potentially explaining why S-EABR
441 mRNA-LNP induced larger increases in antibody titers at lower doses. Co-delivery of
442 multiple mRNAs also poses an obstacle for vaccine manufacturing, whereas COVID-
443 19 and other mRNA vaccines could be easily modified to generate eVLPs by adding
444 a short sequence containing EABR and EPM motifs to the cytoplasmic domains of the
445 encoded immunogens. mRNA delivery of a trimerized RBD-ferritin fusion construct,
446 which should result in secretion of non-enveloped ferritin nanoparticles displaying
447 trimeric RBDs without cell surface expression of RBDs, has also been reported (Sun
448 et al., 2021). This approach was not compared to a conventional S mRNA-LNP-based
449 immunogen, highlighting the need for comparison studies of different vaccine
450 approaches to elucidate the individual effects of antigen presentation on cell surfaces
451 and virus-like nanoparticles on the magnitude and quality of immune responses.
452
453 In summary, we present a novel technology to efficiently generate eVLPs for vaccine
454 and other therapeutic applications. We demonstrate that an mRNA vaccine encoding
455 SARS-CoV-2 spike-EABR eVLPs elicits antibody responses with enhanced potency
456 and breadth compared to conventional vaccine strategies in mice, which warrants
457 further investigation in other preclinical animal models and humans as a vaccine
458 strategy.

459 **Acknowledgements**

460 We thank J. Vielmetter and the Caltech Protein Expression Center for assistance with
461 protein production, K. Dam for biotinylated proteins for ELISAs, M. Anaya for a BirA
462 expression plasmid, and J. Bloom (Fred Hutchinson) and P. Bieniasz (Rockefeller
463 University) for neutralization assay reagents. We thank J. Keeffe, A. West, Y. Tam
464 (Acuitas Therapeutics), C. Barnes (Stanford), H. Kleanthous (Bill and Melinda Gates
465 Foundation), B. Wold, G. Tolomiczenko, and the Caltech Merkin Institute for
466 Translational Research for helpful discussions and A. West for careful reading of the
467 manuscript. Electron tomography was performed in the Caltech Cryo-EM Center with
468 assistance from S. Chen. We thank Labcorp Drug Development–Antibody Reagents
469 and Vaccines (Denver, PA) (formerly Covance, Inc.) for mouse immunization studies,
470 BIOQUAL, Inc. (Rockville, MD) for PRNT50 assays, and R. Sukhovershin and
471 RNAcore (Houston Methodist Research Institute) for synthesis of mRNAs and helpful
472 discussion. Figures 1A and 3A were created with Biorender.com. This work was
473 supported by the Bill and Melinda Gates Foundation INV-034638 (P.J.B.), the Caltech
474 Merkin Institute (P.J.B.), the George Mason University Fast Grants (P.J.B.), the
475 Rothenberg Innovation Initiative (RI²) (P.J.B.), and Wellcome Leap (P.J.B.). M.A.G.H.
476 was supported by an NIH Director's Early Independence Award (FAIN#
477 DP5OD033362).

478

479 **Author contributions:**

480 M.A.G.H. and P.J.B. conceived the study, acquired funding, analyzed the data, and
481 wrote the manuscript with contributions from other authors (Z.Y., P.J.C.L.). M.A.G.H.
482 and K.E.H.T. generated, expressed, and evaluated EABR constructs by Western blot
483 and flow cytometry analysis. M.A.G.H., K.E.H.T., P.N.P.G., L.M.K., and K.N.S.

484 evaluated serum antibody responses from immunized mice by ELISA and
485 neutralization assays. Z.Y. performed cryo-electron tomography and interpreted
486 results. A.A.C. prepared S-mi3 immunogens for immunization studies in mice. W.J.M.
487 and P.J.C.L. prepared mRNA-LNP for immunization studies in mice.

488

489 **Competing interests**

490 M.A.G.H. and P.J.B. are inventors on a US patent application filed by the California
491 Institute of Technology that covers the EABR technology described in this work.
492 W.J.M. and P.J.C.L. are employees of Acuitas Therapeutics, a company developing
493 lipid nanoparticle delivery technology; P.J.C.L. holds equity in Acuitas Therapeutics.

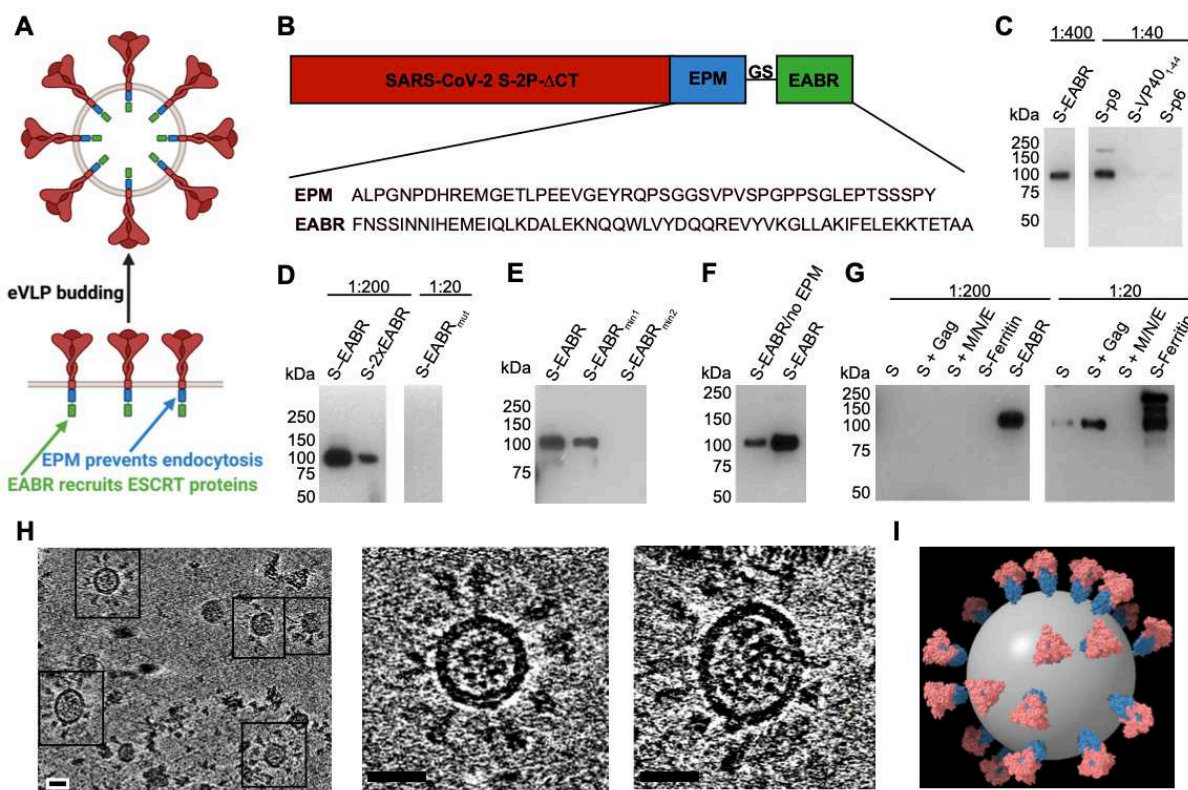
494

495 **Data availability**

496 All data are available in the main text or the supplementary information. Materials are
497 available upon request to the corresponding authors with a signed material transfer
498 agreement. This work is licensed under a Creative Commons Attribution 4.0
499 International (CC BY 4.0) license, which permits unrestricted use, distribution, and
500 reproduction in any medium, provided the original work is properly cited. To view a
501 copy of this license, visit <https://creativecommons.org/licenses/by/4.0/>. This license
502 does not apply to figures/photos/artwork or other content included in the article that is
503 credited to a third party; obtain authorization from the rights holder before using such
504 material.

505

506



508 **Figure 1 EABR insertion into the cytoplasmic tail of membrane proteins results**
509 **in eVLP budding and release.**

510 (A) Schematic of membrane-bound SARS-CoV-2 S proteins on the cell surface
511 containing cytoplasmic tail EPM and EABR insertions that induce budding of an eVLP
512 comprising a lipid bilayer with embedded S proteins.

513

514 (B) Sequence information for S-EABR construct. Top: The SARS-CoV-2 S protein
515 (including a furin cleavage site, 2P stabilizing substitutions, the D614G substitution,
516 and Δ CT, a cytoplasmic tail deletion) is fused to an EPM sequence, a (Gly)₃Ser (GS)
517 spacer, and an EABR sequence. EPM = Endocytosis prevention motif. GS = (Gly)₃Ser
518 linker. EABR = ESCRT- and ALIX-binding region. Bottom: EPM and EABR sequence
519 information.

520

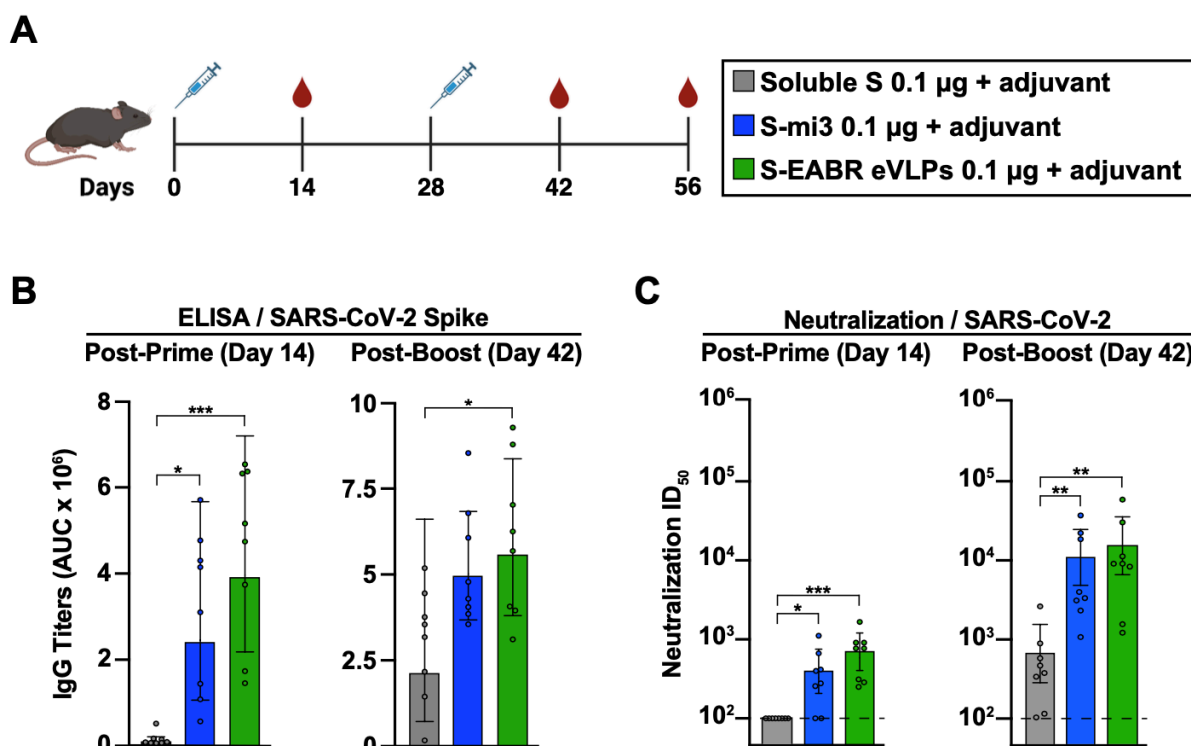
521 (C-G) Western blot analysis detecting SARS-CoV-2 S1 protein on eVLPs purified by
522 ultracentrifugation on a 20% sucrose cushion from transfected Expi293F cell culture
523 supernatants. (C) Cells were transfected with S-EABR, S-p9, S-VP40₁₋₄₄, or S-p6
524 constructs. The purified S-EABR eVLP sample was diluted 1:400 (left), while S-p9, S-
525 VP40₁₋₄₄, and S-p6 samples were diluted 1:40 (right). Comparison of band intensities
526 between lanes suggest that the S-EABR eVLP sample contained ~10-fold higher
527 levels of S1 protein than the S-p9 sample and >10-fold higher levels than the S-VP40<sub>1-
528 44</sub> and S-p6 samples. (D) Cells were transfected with S-EABR, S-2xEABR (left) or S-
529 EABR_{mut} constructs (right). Purified S-EABR and S-2xEABR eVLP samples were
530 diluted 1:200, while the S-EABR_{mut} sample was diluted 1:20. (E) Cells were transfected
531 with S-EABR, S-EABR_{min1}, or S-EABR_{min2} constructs. Purified eVLP samples were
532 diluted 1:200. (F) Cells were transfected with S-EABR/no EPM or S-EABR constructs.
533 Purified eVLP samples were diluted 1:200. (G) Cells were transfected to express S
534 alone, S plus the HIV-1 Gag protein, S plus the SARS-CoV-2 M, N, and E proteins, an
535 S-ferritin fusion protein, or S-EABR. Purified eVLP samples were diluted 1:200 (left)
536 or 1:20 (right). Comparison of band intensities between lanes suggest that the S-EABR
537 eVLP sample contained >10-fold higher levels of S1 protein than S alone, S plus Gag,
538 and S plus M, N, E.

539
540 (H) Computationally-derived tomographic slices (8.1 nm) of S-EABR eVLPs derived
541 from cryo-ET imaging of S-EABR eVLPs purified from transfected cell culture
542 supernatants by ultracentrifugation on a 20% sucrose cushion and SEC. Left:
543 Representative eVLPs are highlighted in boxes. Middle and right: Close-ups of
544 individual eVLPs. Scale bars = 30 nm.

545 (I) Model of a representative S-EABR eVLP derived from a cryo-ET reconstruction
546 (Movie S1). Coordinates of an S trimer (PDB 6VXX) (Walls et al., 2020) were fit into
547 protruding density on the best resolved half of an eVLP and the remainder of the eVLP
548 was modeled assuming a similar distribution of trimers. The position of the lipid bilayer
549 is shown as a 55 nm gray sphere.

550

551



552

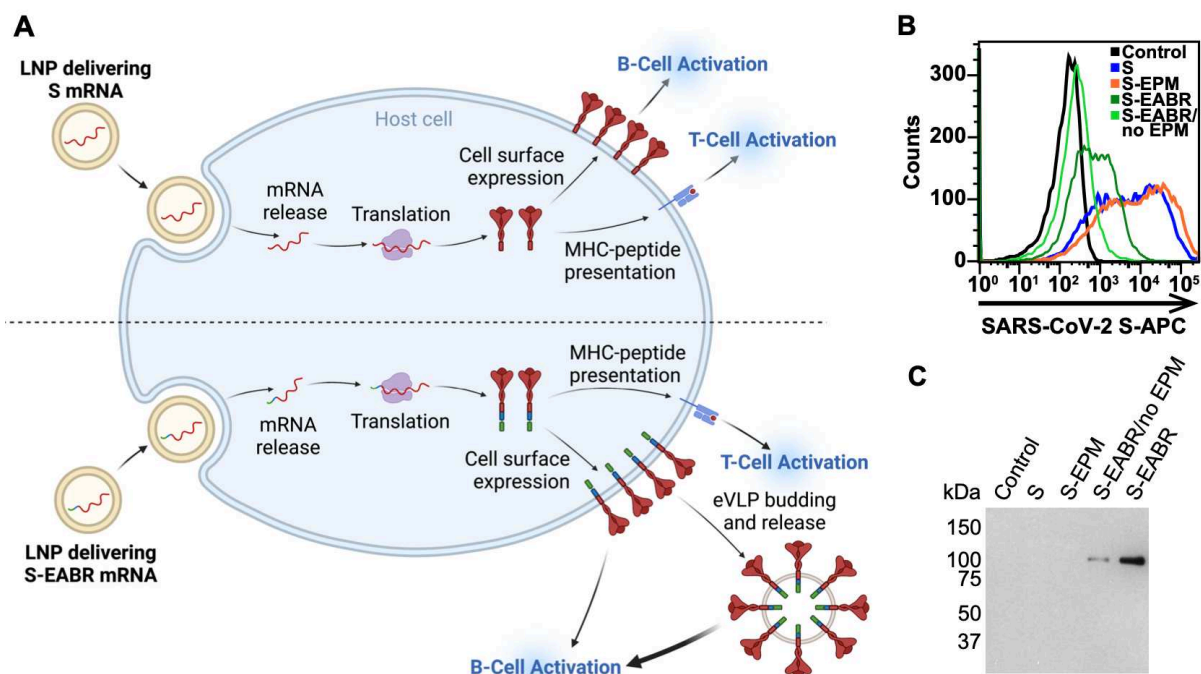
553 **Figure 2 Purified S-EABR eVLPs induce potent antibody responses in mice.**

554 (A) Immunization schedule. C57BL/6 mice were immunized with soluble S (purified S
555 trimer) (gray), S-mi3 (S trimer ectodomains covalently attached to mi3, a 60-mer
556 protein nanoparticle) (blue), or S-EABR eVLPs (green).

557

558 (B-C) ELISA and neutralization data from the indicated time points for antisera from
559 individual mice (colored circles) presented as the geometric mean (bars) and standard
560 deviation (horizontal lines). ELISA results are shown as area under the curve (AUC);
561 neutralization results are shown as half-maximal inhibitory dilutions (ID₅₀ values).
562 Dashed horizontal lines correspond to the background values representing the limit of
563 detection for neutralization assays. Significant differences between cohorts linked by
564 horizontal lines are indicated by asterisks: p<0.05 = *, p<0.01 = **, p<0.001 = ***.

565
566



568 **Figure 3 mRNA-mediated delivery of the S-EABR construct results in cell
569 surface expression and eVLP assembly.**

570 (A) Schematic comparison of mRNA-LNP delivery of S (as in COVID-19 mRNA
571 vaccines) (top) versus delivery of an S-EABR construct (bottom). Both approaches
572 generate S peptides displayed on class I MHC molecules for CD8⁺ T cell recognition
573 and result in presentation of S antigens on cell surfaces. The S-EABR approach also
574 results in budding and release of eVLPs displaying S antigens.

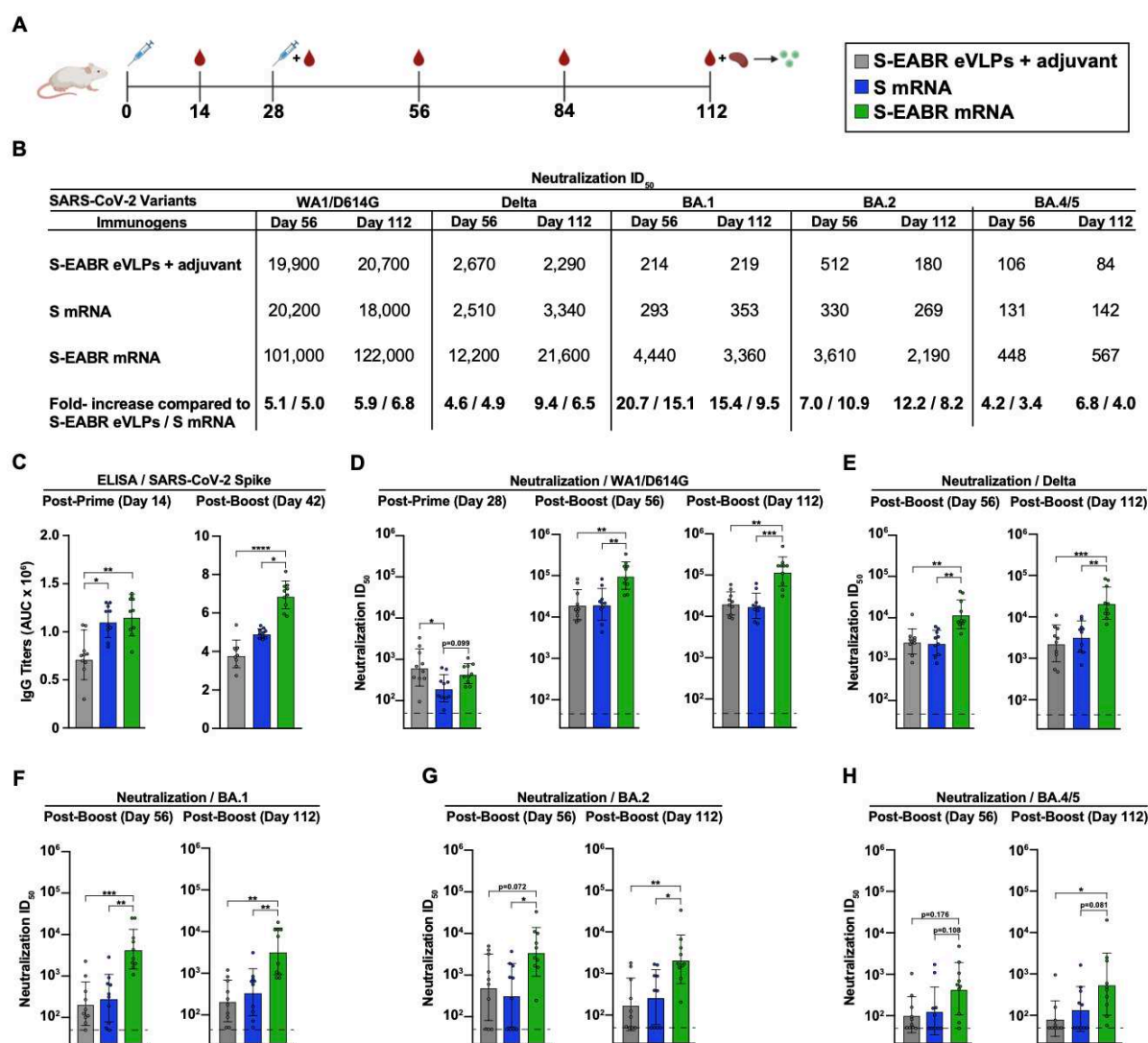
575

576 (B) Flow cytometry analysis of SARS-CoV-2 S cell surface expression on HEK293T
577 cells that were untransfected (black) or transfected with mRNAs encoding S (blue), S-
578 EPM (orange), S-EABR (dark green), or S-EABR/no EPM (light green) constructs.

579

580 (C) Western blot analysis of eVLPs purified by ultracentrifugation on a 20% sucrose
581 cushion from supernatants from the transfected cells in panel B. Purified eVLP
582 samples were diluted 1:10.

583



584
 585
 586 **Figure 4 mRNA-LNP encoding S-EABR eVLPs induce potent antibody
 587 responses in mice.**

588 (A) Immunization schedule. BALB/c mice were immunized with purified S-EABR
 589 eVLPs (1 μ g S protein) plus adjuvant (gray), 2 μ g of mRNA-LNP encoding S (blue), or
 590 2 μ g of mRNA-LNP encoding S-EABR (green). On day 112, spleens were harvested
 591 from immunized mice for ELISpot analysis.

592

593 (B) Neutralization data from indicated time points for antisera presented as geometric
 594 mean half-maximal inhibitory dilution (ID₅₀) values against SARS-CoV-2 WA1/D614G,
 595 Delta, Omicron BA.1, Omicron BA.2, and Omicron BA.4/5 pseudoviruses. Bottom

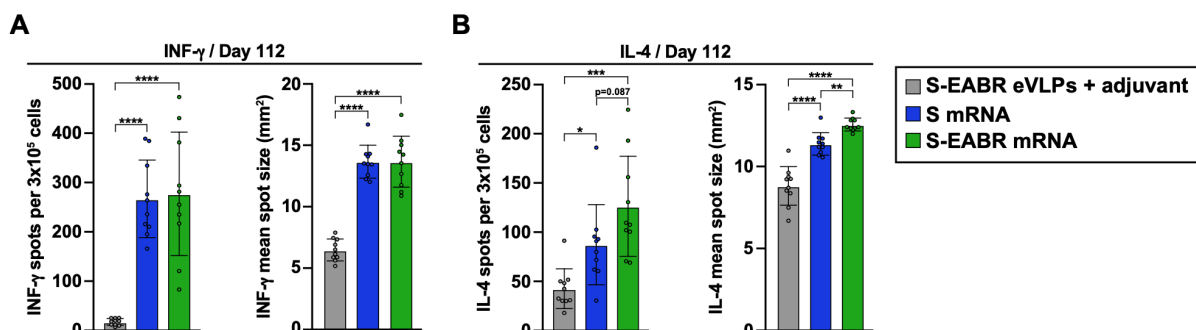
596 horizontal row shows the fold increases for geometric mean ID₅₀ values for mice that
597 received S-EABR mRNA-LNP compared to mice that received purified S-EABR
598 eVLPs or S mRNA-LNP.

599

600 (C) ELISA data from the indicated time points for antisera from individual mice (colored
601 circles) presented as the geometric mean (bars) and standard deviation (horizontal
602 lines). ELISAs evaluated binding of SARS-CoV-2 S trimers; results are shown as area
603 under the curve (AUC).

604

605 (D-H) Neutralization data from the indicated time points for antisera from individual
606 mice (colored circles) presented as the geometric mean (bars) and standard deviation
607 (horizontal lines). Neutralization results against SARS-CoV-2 WA1/D614G (D), Delta
608 (E), Omicron BA.1 (F), Omicron BA.2 (G), and Omicron BA.4/5 (H) pseudoviruses are
609 shown as ID₅₀ values. Dashed horizontal lines correspond to the background values
610 representing the limit of detection for neutralization assays. Significant differences
611 between cohorts linked by horizontal lines are indicated by asterisks: p<0.05 = *,
612 p<0.01 = **, p<0.001 = ***, p<0.0001 = ****.



613
614
615 **Figure 5 mRNA-LNP encoding S-EABR eVLPs induce potent T cell responses in**

616 **mice.**

617 (A-B) ELISpot assay data for SARS-CoV-2 S-specific INF- γ (A) and IL-4 (B) responses
618 of splenocytes from BALB/c mice that were immunized with purified S-EABR eVLPs
619 (1 μ g S protein) plus adjuvant (gray), 2 μ g of mRNA-LNP encoding S (blue), or 2 μ g
620 of mRNA-LNP encoding S-EABR (green). Results are shown as spots per 3×10^5 cells
621 (left) and mean spot sizes (right) for individual mice (colored circles) presented as the
622 mean (bars) and standard deviation (horizontal lines). Significant differences between
623 cohorts linked by horizontal lines are indicated by asterisks: $p < 0.05 = *$, $p < 0.01 = **$,
624 $p < 0.001 = ***$, $p < 0.0001 = ****$.

625
626

627
628

Supplemental Information

629 **Title: ESCRT recruitment to mRNA-encoded SARS-CoV-2 spike induces virus-
630 like particles and enhanced antibody responses**

631

632 **Authors:** Magnus A. G. Hoffmann^{1*}, Zhi Yang^{1‡}, Kathryn E. Huey-Tubman¹,
633 Alexander A. Cohen¹, Priyanthi N. P. Gnanapragasam¹, Leesa M. Nakatomi¹, Kaya
634 N. Storm¹, Woohyun J. Moon², Paulo J.C. Lin², Pamela J. Bjorkman^{1*}

635

636 **Affiliations:**

637 ¹Division of Biology and Biological Engineering, California Institute of Technology,
638 Pasadena, CA 91125, USA

639 ²Acuitas Therapeutics, Vancouver, BC, V6T 1Z3, CANADA

640 [‡]Present address: Department of Molecular and Cell Biology, University of California,
641 Berkeley, CA 94720, USA

642

643 *To whom correspondence should be addressed: Email: mhoffman@caltech.edu,
644 bjorkman@caltech.edu

645

646

647 **Methods**

648 **Design of EABR constructs**

649 The EABR domain (residues 160-217) of the human CEP55 protein was fused to the
650 C-terminus of the SARS-CoV-2 S protein (WA1/D614G) separated by a 4-residue
651 (Gly)₃Ser (GS) linker to generate S-EABR/no EPM. This construct contained the native
652 furin cleavage site, 2P stabilizing mutations (Pallesen et al., 2017), and the C-terminal
653 21 residues were truncated to remove an ER-retention signal (McBride et al., 2007).
654 The S-EABR construct was generated by inserting residues 243-290 of mouse FcgRII-
655 B1 upstream of the 4-residue GS linker and the EABR domain. The S-EABR_{min1} and
656 S-EABR_{min2} constructs encoded residues 170-217 and 170-208 of CEP55,
657 respectively. EABR constructs were also generated for HIV-1 Env_{YU2} and human
658 CCR5. S-p6, S-VP40₁₋₄₄, and S-p9 were generated by replacing the EABR domain
659 gene with sequences encoding HIV-1 p6 (isolate HXB2), EBOV VP40 (residues 1-44;
660 Zaire EBOV), and EIAV p9 (strain Wyoming), respectively. The S-ferritin construct was
661 designed as described (Powell et al., 2021) by fusing genes encoding the ectodomain
662 of SARS-CoV-2 S WA1/D614G containing a furin cleavage site and 2P mutations, and
663 *Helicobacter pylori* ferritin, separated by a 3-residue Ser-Gly-Gly linker. All constructs
664 were cloned into the p3bNC expression plasmid.

665

666 **Production of EABR eVLPs**

667 EABR eVLPs were generated by transfecting Expi293F cells (Gibco) cultured in
668 Expi293F expression media (Gibco) on an orbital shaker at 37°C and 8% CO₂. Gag-
669 based eVLPs were produced by co-transfecting Expi293F cells with a plasmid
670 expressing Rev-independent HIV-1 Gag-Pol (pHDM-Hgpm2 plasmid; PlasmID
671 Repository, Harvard Medical School) and SARS-CoV-2 S, HIV-1 Env_{YU2}, or CCR5,

672 respectively, at a ratio of 1:1. SARS-CoV-2 M/N/E-based eVLPs were produced by
673 co-transfected Expi293F cells with plasmids expressing the SARS-CoV-2 M, N, E,
674 and S proteins at a ratio of 1:1:1:1. To enable interactions between M, N, E, and S,
675 we transfected full-length S with an untruncated cytoplasmic domain. 72 hours post-
676 transfection, cells were centrifuged at 400 x g for 10 min, supernatants were passed
677 through a 0.45 µm syringe filter and concentrated using Amicon Ultra-15 centrifugal
678 filters with 100 kDa molecular weight cut-off (Millipore). eVLPs were purified by
679 ultracentrifugation at 50,000 rpm (135,000 x g) for 2 hours at 4°C using a TLA100.3
680 rotor and a Optima™ TLX ultracentrifuge (Beckman Coulter) on a 20% w/v sucrose
681 cushion. Supernatants were removed and pellets were re-suspended in 200 µL sterile
682 PBS at 4°C overnight. To remove residual cell debris, samples were centrifuged at
683 10,000 x g for 10 min and supernatants were collected. For in vivo studies and cryo-
684 ET, eVLPs were further purified by SEC using a Superose 6 10/300 column (GE
685 Healthcare) equilibrated with PBS. Peak fractions corresponding to S-EABR eVLPs
686 were combined and concentrated to 250-500 µL in Amicon Ultra-4 centrifugal filters
687 with 100 kDa molecular weight cut-off. Samples were aliquoted and stored at -20°C.
688

689 **Protein expression**

690 Soluble SARS-CoV-2 S-6P trimers (WA1/D614G) (Hsieh et al., 2020) and RBDs were
691 expressed as described (Cohen et al., 2022; Wang et al., 2022). Briefly, Avi/His-
692 tagged proteins were purified from transiently-transfected Expi293F cells (Gibco) by
693 nickel affinity chromatography and SEC (Barnes et al., 2020; Cohen et al., 2022; Wang
694 et al., 2022). Peak fractions corresponding to S-6P or RBD proteins were pooled,
695 concentrated, and stored at 4°C. Biotinylated proteins for ELISAs were generated by
696 co-transfection of Avi/His-tagged S-6P and RBD constructs with a plasmid encoding

697 an endoplasmic reticulum-directed BirA enzyme (kind gift from Michael Anaya,
698 Caltech). S-6P constructs with a C-terminal SpyTag003 tag (Keeble et al., 2019) were
699 expressed for covalent coupling to a 60-mer protein nanoparticle (SpyCatcher003-
700 mi3) using the SpyCatcher-SpyTag system (Brune et al., 2016; Zakeri et al., 2012).

701

702 **Preparation of SpyCatcher003-mi3 nanoparticles**

703 SpyCatcher003-mi3 (Cohen et al., 2021) displaying SpyTagged SARS-CoV-2 S-6P
704 trimers were prepared as described (Cohen et al., 2021; Cohen et al., 2022). Briefly,
705 SpyCatcher003-mi3 subunits with N-terminal 6xHis tags were expressed in BL21
706 (DE3)-RIPL *E. coli* (Agilent). Bacterial cell pellets were lysed using a cell disruptor in
707 the presence of 2.0 mM PMSF (Sigma). Lysates were centrifuged at 21,000 x g for 30
708 min, and supernatants were collected and filtered through a 0.2 µm filter.
709 SpyCatcher003-mi3 was purified by Ni-NTA chromatography using a pre-packed
710 HisTrap™ HP column (GE Healthcare), concentrated in Amicon Ultra-15 centrifugal
711 filters with 30 kDa molecular weight cut-off (Millipore), and purified by SEC on a HiLoad
712 16/600 Superdex 200 column (GE Healthcare) equilibrated with TBS. S-mi3
713 nanoparticles were generated by incubating purified SpyCatcher003-mi3 with a 3-fold
714 molar excess of purified SpyTagged S-6P trimer overnight at 4°C in TBS. Conjugated
715 S-mi3 nanoparticles were separated from uncoupled S-6P trimers by SEC using a
716 Superose 6 10/300 column (GE Healthcare) equilibrated with PBS. Fractions
717 corresponding to conjugated S-mi3 were identified by sodium dodecyl sulfate
718 polyacrylamide gel electrophoresis (SDS-PAGE) and pooled.

719

720

721

722 **Western blot analysis**

723 The presence of SARS-CoV-2 S, HIV-1 Env_{YU2}, and CCR5 on purified eVLPs was
724 detected by Western blot analysis. Samples were diluted in SDS-PAGE loading buffer
725 under reducing conditions, separated by SDS-PAGE, and transferred to nitrocellulose
726 membranes (0.2 µm) (GE Healthcare). The following antibodies were used for
727 detecting SARS-CoV-2 S, HIV-1 Env_{YU2}, and CCR5: rabbit anti-SARS-CoV-2 S1
728 protein (PA5-81795; ThermoFisher) at 1:2,500, the human anti-HIV-1 Env broadly
729 neutralizing antibody 10-1074 (Mouquet et al., 2012) (expressed in-house) at
730 1:10,000, rat anti-CCR5 (ab111300; Abcam) at 1:2,000, HRP-conjugated mouse anti-
731 rabbit IgG (211-032-171; Jackson ImmunoResearch) at 1:10,000, HRP-conjugated
732 goat anti-human IgG (2014-05; Southern Biotech) at 1:8,000, and HRP-conjugated
733 mouse anti-rat IgG (3065-05; Southern Biotech) at 1:10,000. Protein bands were
734 visualized using ECL Prime Western Blotting Detection Reagent (GE Healthcare).

735

736 For in vivo studies, the amount of SARS-CoV-2 S on S-EABR eVLPs was determined
737 by quantitative Western blot analysis. Various dilutions of SEC-purified S-EABR eVLP
738 samples and known amounts of soluble SARS-CoV-2 S1 protein (Sino Biological)
739 were separated by SDS-PAGE and transferred to nitrocellulose membranes (GE
740 Healthcare). SARS-CoV-2 S was detected as described above. Band intensities of the
741 SARS-CoV-2 S1 standards and S-EABR eVLP sample dilutions were measured using
742 ImageJ to determine S concentrations. The S1 protein concentrations determined for
743 S-EABR samples were multiplied by a factor of 1.8 to account for the difference in
744 molecular weight between S1 and the full-length S protein.

745

746

747 **Cryo-ET of S-EABR eVLPs**

748 SEC-purified S-EABR eVLPs were prepared on grids for cryo-ET using a Mark IV
749 Vitrobot (ThermoFisher Scientific) operated at 21°C and 100% humidity. 2.5 μ L of
750 sample was mixed with 0.4 μ L of 10 nm fiducial gold beads (Sigma-Aldrich) and
751 applied to 300-mesh Quantifoil R2/2 grids, blotted for 3.5 s, and then plunge-frozen in
752 liquid ethane cooled by liquid nitrogen. Image collections were performed on a 300 kV
753 Titan Krios transmission electron microscope (ThermoFisher Scientific) operating at a
754 nominal 42,000x magnification. Tilt series were collected on a K3 direct electron
755 detector (Gatan) with a pixel size of 2.15 $\text{\AA}\cdot\text{pixel}^{-1}$ using SerialEM software
756 (Mastronarde, 2005). The defocus range was set to -5 to -8 μm and a total of 120 $\text{e}^- \cdot$
757 \AA^{-2} per tilt series. Images were collected using a dose-symmetric scheme (Hagen et
758 al., 2017) ranging from -60° to 60° with 3° intervals. Tomograms were aligned and
759 reconstructed using IMOD (Mastronarde and Held, 2017).

760

761 To build a model of an S-EABR eVLP, coordinates of a SARS-CoV-2 S trimer (PDB
762 6VXX) were fit into spike densities in the reconstructed tomograms using ChimeraX
763 (Goddard et al., 2018). Positions and orientations of the S protein were adjusted in a
764 hemisphere of the eVLP in which the spike density was of higher quality. A 55 nm
765 sphere was adapted from a cellPACK model (cellPACK ID: HIV-1_0.1.6_6) (Johnson
766 et al., 2015; Johnson et al., 2014) and added to the model to represent the eVLP
767 membrane surface.

768

769 **Neutralization assays**

770 Lentivirus-based SARS-CoV-2 pseudoviruses were generated as described
771 (Crawford et al., 2020; Robbiani et al., 2020) using S proteins from the WA1/D614G,

772 Delta, Omicron BA.1, Omicron BA.2, and Omicron BA.4/5 variants in which the C-
773 terminal 21 residues of the S protein cytoplasmic tails were removed (Crawford et al.,
774 2020). Serum samples from immunized mice were heat-inactivated for 30 min at 56°C.
775 Three-fold serial dilutions of heat-inactivated samples were incubated with
776 pseudoviruses for 1 hour at 37°C, followed by addition of the serum-virus mixtures to
777 pre-seeded HEK293T-ACE2 target cells. After 48-hour incubation at 37°C, BriteLite
778 Plus substrate (Perkin Elmer) was added and luminescence was measured. Half-
779 maximal inhibitory dilutions (ID_{50} s) were calculated using 4-parameter non-linear
780 regression analysis in AntibodyDatabase (West et al., 2013) and ID_{50} values were
781 rounded to three significant figures.

782
783 PRNT₅₀ (50% plaque reduction neutralization test) assays with authentic SARS-CoV-
784 2 virus were performed in a biosafety level 3 facility at BIOQUAL, Inc. (Rockville, MD)
785 as described (Haun et al., 2020). Mouse sera from day 56 post-immunization were
786 diluted 1:20 and then 3-fold serially diluted in culture media (DMEM + 10% FBS +
787 Gentamicin). The diluted samples were incubated with 30 plaque-forming units of wild-
788 type SARS-CoV-2 (USA-WA1/2020, BEI Resources NR-52281; Beta variant, Isolate
789 hCoV-19/South Africa/KRISP-K005325/2020, BEI Resources NR-54009; Delta
790 variant, isolate hCoV-19/USA/MD-HP05647/2021 BEI Resources NR-55674) for 1
791 hour at 37°C. Samples were then added to a confluent monolayer of Vero/TMPRSS2
792 cells in 24-well plates for 1 hour at 37°C in 5% CO₂. 1 mL of culture media with 0.5%
793 methylcellulose was added to each well and plates were incubated for 3 days at 37°C
794 in 5% CO₂. Plates were fixed with ice cold methanol at -20°C for 30 min. Methanol
795 was discarded and plates were stained with 0.2% crystal violet for 30 min at room
796 temperature. Plates were washed once with water and plaques in each well were

797 counted. TCID₅₀ values were calculated using the Reed-Muench formula (Reed and
798 Muench, 1938).

799

800 **ELISAs**

801 Pre-blocked streptavidin-coated Nunc® MaxiSorp™ 384-well plates (Sigma) were
802 coated with 5 µg/mL biotinylated S-6P or RBD proteins in Tris-buffered saline with
803 0.1% Tween 20 (TBS-T) and 3% bovine serum albumin (BSA) for 1 hour at room
804 temperature. Serum samples from immunized mice were diluted 1:100, 4-fold serially
805 diluted in TBS-T/3% BSA, and then added to plates. After a 3-hour incubation at room
806 temperature, plates were washed with TBS-T using an automated plate washer. HRP-
807 conjugated goat anti-mouse IgG (715-035-150; Jackson ImmunoResearch) was
808 diluted 1:100,000 in TBS-T/3% BSA and added to plates for 1 hour at room
809 temperature. After washing with TBS-T, plates were developed using SuperSignal™
810 ELISA Femto Maximal Signal Substrate (ThermoFisher) and absorbance was
811 measured at 425 nm. Area under the curve (AUC) calculations for binding curves were
812 performed using GraphPad Prism 9.3.1 assuming a one-site binding model with a Hill
813 coefficient as described (Cohen et al., 2021).

814

815 **mRNA synthesis**

816 Codon-optimized mRNAs encoding SARS-CoV-2 S, S-EPM, S-EABR/no EPM, and
817 S-EABR constructs were synthesized by RNACore
818 (<https://www.houstonmethodist.org/research-cores/rnacore/>) using proprietary
819 manufacturing protocols. mRNAs were generated by T7 RNA polymerase-mediated
820 in vitro transcription reactions using DNA templates containing the immunogen open
821 reading frame flanked by 5' untranslated region (UTR) and 3' UTR sequences and

822 terminated by an encoded polyA tail. CleanCap 5' cap structures (TriLink) were
823 incorporated into the 5' end co-transcriptionally. Uridine was completely replaced with
824 N1-methyl-pseudouridine to reduce immunogenicity (Kariko et al., 2008). mRNAs
825 were purified by oligo-dT affinity purification and high-performance liquid
826 chromatography (HPLC) to remove double-stranded RNA contaminants (Kariko et al.,
827 2011). Purified mRNAs were stored at –80 °C.

828

829 **mRNA transfections**

830 For mRNA transfections, 10⁶ HEK293T cells were seeded in 6-well plates. After 24
831 hours, cells were transfected with 2 µg mRNA encoding SARS-CoV-2 S, S-EPM, S-
832 EABR/no EPM, or S-EABR constructs using LipofectamineTM MessengerMaxTM
833 transfection reagent (ThermoFisher). 48 hours post-transfection, supernatants were
834 collected and purified for Western blot analysis. Cells were gently detached by
835 pipetting and resuspended in 500 µL PBS. 100 µL were transferred into Eppendorf
836 tubes for flow cytometry analysis of S cell surface expression. Cells were stained with
837 the SARS-CoV-2 antibody C119 (Robbiani et al., 2020) at 5 µg/mL in PBS+ (PBS
838 supplemented with 2% FBS) for 30 min at room temperature in the dark. After two
839 washes in PBS+, samples were stained with an Alexa Fluor[®] 647-conjugated anti-
840 human IgG secondary antibody (A21445; Life Technologies) at a 1:2,000 dilution in
841 PBS+ for 30 min at room temperature in the dark. After two washes in PBS+, cells
842 were resuspended in PBS+ and analyzed by flow cytometry (MACSQuant, Miltenyi
843 Biotec). Results were plotted using FlowJo 10.5.3 software.

844

845

846

847 **LNP encapsulation of mRNAs**

848 Purified N1-methyl-pseudouridine mRNA was formulated in LNP as previously
849 described (Pardi et al., 2015). In brief, 1,2-distearoyl-sn-glycero-3-phosphocholine,
850 cholesterol, a PEG lipid, and an ionizable cationic lipid dissolved in ethanol were
851 rapidly mixed with an aqueous acidic solution containing mRNA using an in-line mixer.
852 The ionizable lipid and LNP composition are described in the international patent
853 application WO2017075531(2017). The post in-line solution was dialyzed with PBS
854 to remove the ethanol and displace the acidic solution. Subsequently, LNP was
855 measured for size (60-65 nm) and polydispersity (PDI < 0.075) by dynamic light
856 scattering (Malvern Nano ZS Zetasizer). Encapsulation efficiencies were >97% as
857 measured by the Quant-iT Ribogreen Assay (Life Technologies).

858

859 **Immunizations**

860 All animal procedures were performed in accordance with IACUC-approved protocols.
861 7-8 week-old female C57BL/6 or BALB/c mice (Charles River Laboratories) were used
862 for immunization experiments with cohorts of 8-10 animals per group. 0.1 µg of protein-
863 based immunogens, including soluble S trimer, S-mi3, and purified S-EABR eVLPs,
864 were administered to C57BL/6 mice by subcutaneous (SC) injections on days 0 and
865 28 in the presence of Sigma adjuvant system (Sigma). 2 µg of S and S-EABR mRNA-
866 LNP were administered to BALB/c mice by intramuscular (IM) injections on days 0 and
867 28. To compare mRNA- and protein-based immunogens, 1 µg purified S-EABR eVLPs
868 were administered IM in the presence of 50% v/v AddaVax™ adjuvant (Invivogen).
869 Serum samples for ELISAs and neutralization assays were obtained on indicated
870 days.

871

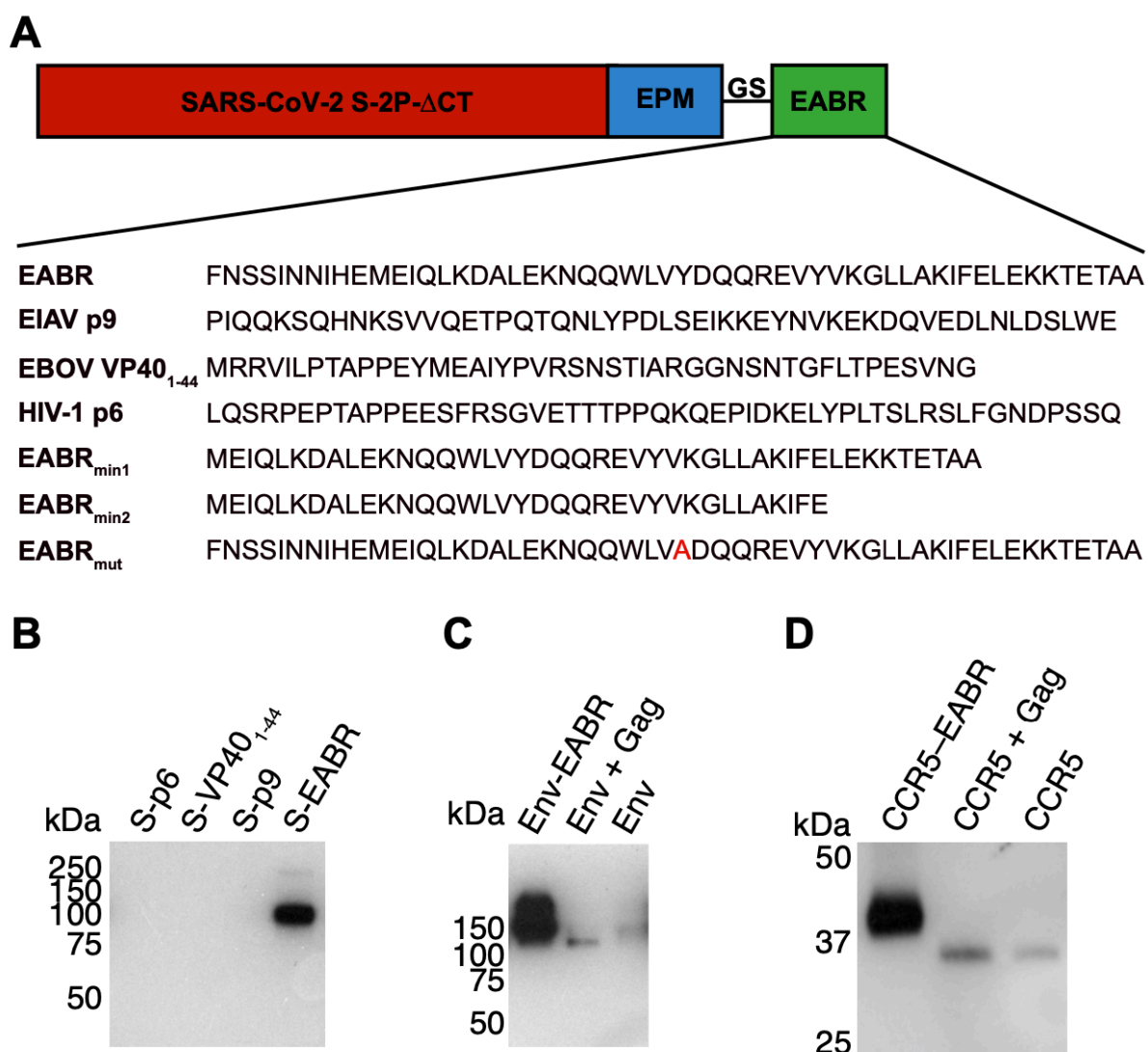
872 **ELISpot assays**

873 Animals were euthanized on day 112 and spleens were collected. Spleens were
874 homogenized using a gentleMACS Octo Dissociator (Miltenyi Biotec). Cells were
875 passed through a 70 μ m tissue screen, centrifuged at 1,500 rpm for 10 min, and
876 resuspended in CTL-TestTM media (ImmunoSpot) containing 1% GlutaMAXTM (Gibco)
877 for ELISpot analysis to evaluate T cell responses. A PepMixTM pool of 315 peptides
878 (15-mers with 11 amino acid overlap) derived from the SARS-CoV-2 S protein (JPT
879 Peptide Technologies) was added to mouse IFN- γ /IL-4 double-color ELISpot plates
880 (ImmunoSpot) at a concentration of 2 μ g/mL. 300,000 cells were added per well, and
881 plates were incubated at 37°C for 24 hours. Biotinylated detection, streptavidin-
882 alkaline phosphatase (AP), and substrate solutions were added according to the
883 manufacturer's guidelines. Plates were gently rinsed with water three times to stop the
884 reactions. Plates were air-dried for two hours in a running laminar flow hood. The
885 number of spots and the mean spot sizes were quantified using a CTL ImmunoSpot
886 S6 Universal-V Analyzer (Immunospot).

887

888 **Statistical analysis**

889 Titer differences between immunized groups of mice for ELISAs and neutralization
890 assays were evaluated for statistical significance using the non-parametric Kruskal-
891 Wallis test followed by Dunn's multiple comparison post hoc test calculated using
892 Graphpad Prism 9.3.1. For ELISpot results, statistically significant differences
893 between immunized groups of mice were determined using analysis of variance
894 (ANOVA) test followed by Tukey's multiple comparison post hoc test calculated using
895 Graphpad Prism 9.3.1.



896
897 **Figure S1 Comparison of EABR-related sequence insertions in the cytoplasmic
898 tail of SARS-CoV-2 S, related to Figure 1.**

899 (A) Top: Schematic of different S-EABR constructs that were compared for their ability
900 to induce eVLP assembly. EPM = Endocytosis prevention motif. GS = (Gly)₃Ser linker.
901 EABR = ESCRT- and ALIX-binding region. Bottom: Amino acid sequences of EABR
902 portion of different constructs.

903

904 (B) Western blot analysis of SARS-CoV-2 S1 protein levels on eVLPs purified by
905 ultracentrifugation on a 20% sucrose cushion from transfected Expi293F cell culture

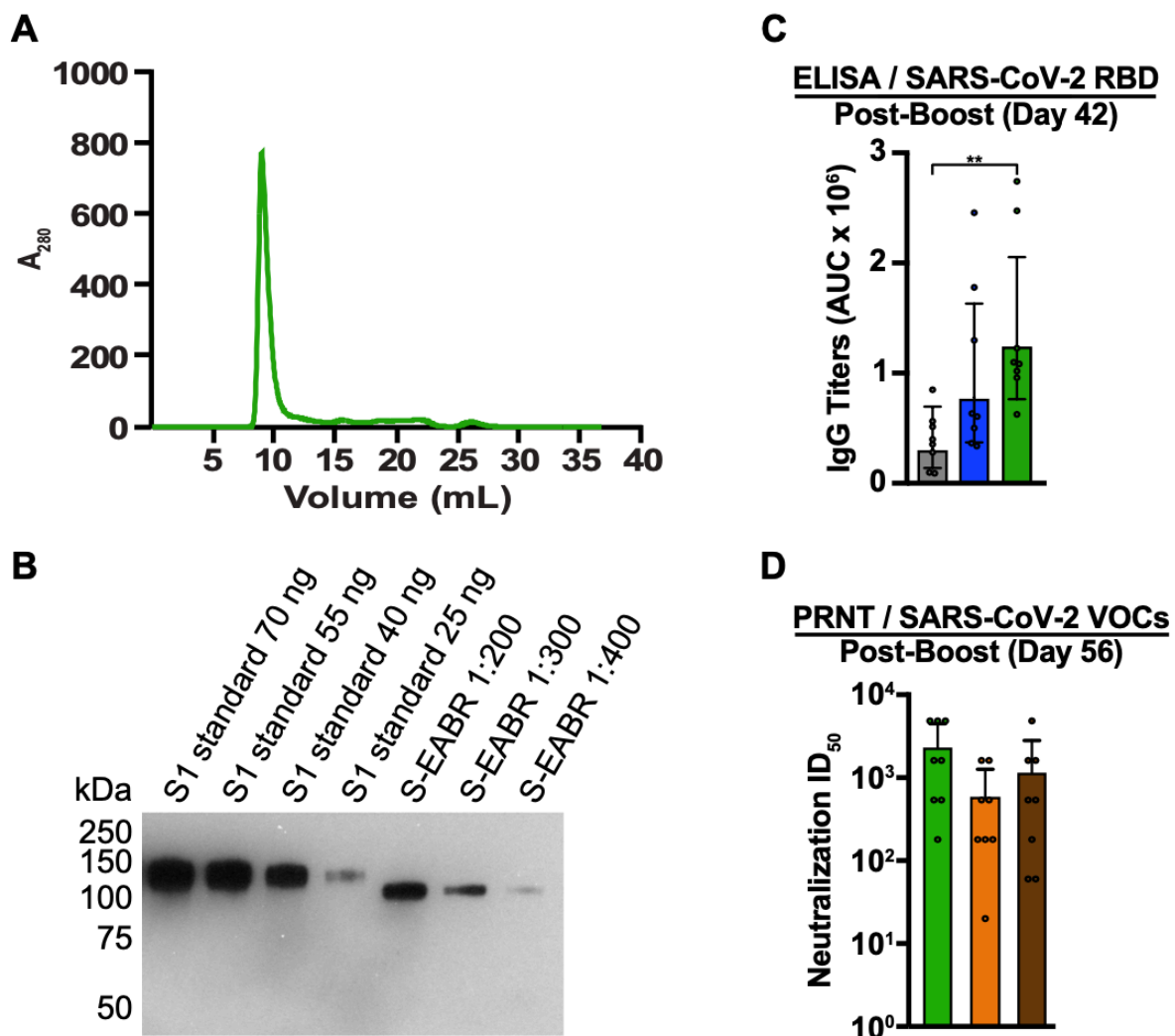
906 supernatants. Cells were transfected with S-p6, S-VP40₁₋₄₄, S-p9, or S-EABR
907 constructs. Purified eVLP samples were diluted 1:400.

908

909 (C) Western blot analysis comparing HIV-1 Env_{YU2} levels in eVLP samples purified
910 from transfected Expi293F cell culture supernatants. Cells were transfected with
911 plasmids encoding Env-EABR, Env plus HIV-1 Gag, or Env alone. Purified eVLP
912 samples were diluted 1:200.

913

914 (D) Western blot analysis comparing CCR5 levels in eVLP samples purified from
915 transfected Expi293F cell culture supernatants. Cells were transfected with plasmids
916 encoding CCR5-EABR, CCR5 plus HIV-1 Gag, or CCR5 alone. Purified eVLP
917 samples were diluted 1:200. The migration difference between CCR5-EABR and
918 CCR5 is due to addition of the EABR sequence (~7 kDa) that increases its molecular
919 mass.



920
921 **Figure S2 Purified S-EABR eVLPs induce potent antibody responses in mice,**

922 **related to Figure 2.**

923 (A) Size exclusion chromatogram of S-EABR eVLPs purified by ultracentrifugation on
924 a 20% sucrose cushion.

925

926 (B) Quantitative Western blot comparing indicated amounts of SARS-CoV-2 S1
927 standards (lanes 1-4) and various dilutions of purified S-EABR eVLPs (lanes 5-7) to
928 determine S protein concentrations in eVLP samples. The S1 standard protein (Sino
929 Biological) was biotinylated and contained a polyhistidine tag, which resulted in a
930 difference in apparent molecular weights for the S1 standards and the S-EABR

931 construct. Band intensities of S1 standards and S-EABR eVLP sample dilutions were
932 measured using ImageJ to determine S concentrations.

933

934 (C) ELISA data from day 42 for antisera from individual mice (colored circles)
935 immunized with soluble S (purified S trimer) (gray), S-mi3 (S trimer ectodomains
936 covalently attached to mi3, a 60-mer protein nanoparticle) (blue), or S-EABR eVLPs
937 (green). Results are shown as area under the curve (AUC) and presented as the
938 geometric mean (bars) and standard deviation (horizontal lines). Significant
939 differences between cohorts linked by horizontal lines are indicated by asterisks:
940 $p < 0.05 = ^*$, $p < 0.01 = ^{**}$.

941

942 (D) PRNT assay results from day 56 for antisera from individual mice (colored circles)
943 immunized with S-EABR eVLPs. Results against the SARS-CoV-2 WA1 (green), Beta
944 (orange), and Delta (brown) variants are shown as TCID₅₀ values (Reed and Muench,
945 1938) and presented as the geometric mean (bars) and standard deviation (horizontal
946 lines).

947

948

949

950

951

952 **References**

953

954 Alberts, B., Johnson, A., Lewis, J., Raff, M., Roberts, K.E., and Walter, P. (2002).
955 Molecular Biology of the Cell, 4th ed.
956 <http://onlinelibrary.wiley.com/doi/10.1002/bmb.2003.494031049999/full> (New York:
957 Garland Science/Taylor & Francis LLC).

958 Baden, L.R., El Sahly, H.M., Essink, B., Kotloff, K., Frey, S., Novak, R., Diemert, D.,
959 Spector, S.A., Roush, N., Creech, C.B., *et al.* (2021). Efficacy and Safety of the
960 mRNA-1273 SARS-CoV-2 Vaccine. *N Engl J Med* 384, 403-416.

961 Barnes, C.O., Jette, C.A., Abernathy, M.E., Dam, K.-M.A., Esswein, S.R., Gristick,
962 H.B., Malyutin, A.G., Sharaf, N.G., Huey-Tubman, K.E., Lee, Y.E., *et al.* (2020).
963 SARS-CoV-2 neutralizing antibody structures inform therapeutic strategies. *Nature*
964 588, 682-687.

965 Barouch, D.H. (2022). Covid-19 Vaccines - Immunity, Variants, Boosters. *N Engl J
966 Med* 387, 1011-1020.

967 Brune, K.D., Leneghan, D.B., Brian, I.J., Ishizuka, A.S., Bachmann, M.F., Draper,
968 S.J., Biswas, S., and Howarth, M. (2016). Plug-and-Display: decoration of Virus-Like
969 Particles via isopeptide bonds for modular immunization. *Scientific reports* 6, 19234.

970 Chen, R.E., Zhang, X., Case, J.B., Winkler, E.S., Liu, Y., VanBlargan, L.A., Liu, J.,
971 Errico, J.M., Xie, X., Suryadevara, N., *et al.* (2021). Resistance of SARS-CoV-2
972 variants to neutralization by monoclonal and serum-derived polyclonal antibodies.
973 *Nat Med* 10.1038/s41591-021-01294-w.

974 Chen, Y., Zhao, X., Zhou, H., Zhu, H., Jiang, S., and Wang, P. (2022). Broadly
975 neutralizing antibodies to SARS-CoV-2 and other human coronaviruses. *Nat Rev
976 Immunol* 10.1038/s41577-022-00784-3.

977 Cohen, A.A., Gnanapragasam, P.N.P., Lee, Y.E., Hoffman, P.R., Ou, S., Kakutani,
978 L.M., Keeffe, J.R., Wu, H.J., Howarth, M., West, A.P., *et al.* (2021). Mosaic
979 nanoparticles elicit cross-reactive immune responses to zoonotic coronaviruses in
980 mice. *Science* 371, 735-741.

981 Cohen, A.A., van Doremalen, N., Greaney, A.J., Andersen, H., Sharma, A., Starr,
982 T.N., Keeffe, J.R., Fan, C., Schulz, J.E., Gnanapragasam, P.N.P., *et al.* (2022).
983 Mosaic RBD nanoparticles protect against challenge by diverse sarbecoviruses in
984 animal models. *Science* 377, eabq0839.

985 Corbett, K.S., Edwards, D.K., Leist, S.R., Abiona, O.M., Boyoglu-Barnum, S.,
986 Gillespie, R.A., Himansu, S., Schafer, A., Ziwawo, C.T., DiPiazza, A.T., *et al.* (2020).
987 SARS-CoV-2 mRNA vaccine design enabled by prototype pathogen preparedness.
988 *Nature* 586, 567-571.

989 Cox, M.M., and Hollister, J.R. (2009). FluBlok, a next generation influenza vaccine
990 manufactured in insect cells. *Biologicals* 37, 182-189.

991 Crawford, K.H.D., Eguia, R., Dingens, A.S., Loes, A.N., Malone, K.D., Wolf, C.R.,
992 Chu, H.Y., Tortorici, M.A., Veesler, D., Murphy, M., *et al.* (2020). Protocol and
993 Reagents for Pseudotyping Lentiviral Particles with SARS-CoV-2 Spike Protein for
994 Neutralization Assays. *Viruses* 12.

995 Fisher, R.D., Chung, H.Y., Zhai, Q., Robinson, H., Sundquist, W.I., and Hill, C.P.
996 (2007). Structural and biochemical studies of ALIX/AIP1 and its role in retrovirus
997 budding. *Cell* 128, 841-852.

998 Fujii, K., Munshi, U.M., Ablan, S.D., Demirov, D.G., Soheilian, F., Nagashima, K.,
999 Stephen, A.G., Fisher, R.J., and Freed, E.O. (2009). Functional role of Alix in HIV-1
1000 replication. *Virology* 391, 284-292.

1001 Goddard, T.D., Huang, C.C., Meng, E.C., Pettersen, E.F., Couch, G.S., Morris, J.H.,
1002 and Ferrin, T.E. (2018). UCSF ChimeraX: Meeting modern challenges in
1003 visualization and analysis. *Protein Sci* 27, 14-25.

1004 Gruell, H., Vanshylla, K., Tober-Lau, P., Hillus, D., Schommers, P., Lehmann, C.,
1005 Kurth, F., Sander, L.E., and Klein, F. (2022). mRNA booster immunization elicits
1006 potent neutralizing serum activity against the SARS-CoV-2 Omicron variant. *Nat Med*
1007 28, 477-480.

1008 Hachmann, N.P., Miller, J., Collier, A.Y., Ventura, J.D., Yu, J., Rowe, M., Bondzie,
1009 E.A., Powers, O., Surve, N., Hall, K., *et al.* (2022). Neutralization Escape by SARS-
1010 CoV-2 Omicron Subvariants BA.2.12.1, BA.4, and BA.5. *N Engl J Med* 387, 86-88.

1011 Hagen, W.J.H., Wan, W., and Briggs, J.A.G. (2017). Implementation of a cryo-
1012 electron tomography tilt-scheme optimized for high resolution subtomogram
1013 averaging. *J Struct Biol* 197, 191-198.

1014 Haun, B.K., Lai, C.Y., Williams, C.A., Wong, T.A.S., Lieberman, M.M., Pessant, L.,
1015 Andersen, H., and Lehrer, A.T. (2020). CoVaccine HT Adjuvant Potentiates Robust
1016 Immune Responses to Recombinant SARS-CoV-2 Spike S1 Immunization. *Front
1017 Immunol* 11, 599587.

1018 Heath, P.T., Galiza, E.P., Baxter, D.N., Boffito, M., Browne, D., Burns, F., Chadwick,
1019 D.R., Clark, R., Cosgrove, C., Galloway, J., *et al.* (2021). Safety and Efficacy of
1020 NVX-CoV2373 Covid-19 Vaccine. *N Engl J Med* 385, 1172-1183.

1021 Hoffmann, M.A.G., Bar-On, Y., Yang, Z., Gristick, H.B., Gnanapragasam, P.N.P.,
1022 Vielmetter, J., Nussenzweig, M.C., and Bjorkman, P.J. (2020). Nanoparticles
1023 presenting clusters of CD4 expose a universal vulnerability of HIV-1 by mimicking
1024 target cells. *Proc Natl Acad Sci U S A* 117, 18719-18728.

1025 Hogan, M.J., and Pardi, N. (2022). mRNA Vaccines in the COVID-19 Pandemic and
1026 Beyond. *Annu Rev Med* 73, 17-39.

1027 Hsieh, C.L., Goldsmith, J.A., Schaub, J.M., DiVenere, A.M., Kuo, H.C., Javanmardi,
1028 K., Le, K.C., Wrapp, D., Lee, A.G., Liu, Y., *et al.* (2020). Structure-based design of
1029 prefusion-stabilized SARS-CoV-2 spikes. *Science* 369, 1501-1505.

1030 Johnson, G.T., Autin, L., Al-Alusi, M., Goodsell, D.S., Sanner, M.F., and Olson, A.J.
1031 (2015). cellPACK: a virtual mesoscope to model and visualize structural systems
1032 biology. *Nat Methods* 12, 85-91.

1033 Johnson, G.T., Goodsell, D.S., Autin, L., Forli, S., Sanner, M.F., and Olson, A.J.
1034 (2014). 3D molecular models of whole HIV-1 virions generated with cellPACK.
1035 *Faraday Discuss* 169, 23-44.

1036 Joyce, M.G., Chen, W.H., Sankhala, R.S., Hajduczki, A., Thomas, P.V., Choe, M.,
1037 Martinez, E.J., Chang, W.C., Peterson, C.E., Morrison, E.B., *et al.* (2021). SARS-
1038 CoV-2 ferritin nanoparticle vaccines elicit broad SARS coronavirus immunogenicity.
1039 *Cell reports* 37, 110143.

1040 Karbiener, M., Farcet, M.R., Zollner, A., Masuda, T., Mori, M., Moschen, A.R., and
1041 Kreil, T.R. (2022). Calibrated comparison of SARS-CoV-2 neutralizing antibody
1042 levels in response to protein-, mRNA-, and vector-based COVID-19 vaccines. *NPJ
1043 Vaccines* 7, 22.

1044 Kariko, K., Muramatsu, H., Ludwig, J., and Weissman, D. (2011). Generating the
1045 optimal mRNA for therapy: HPLC purification eliminates immune activation and
1046 improves translation of nucleoside-modified, protein-encoding mRNA. *Nucleic Acids
1047 Res* 39, e142.

1048 Kariko, K., Muramatsu, H., Welsh, F.A., Ludwig, J., Kato, H., Akira, S., and
1049 Weissman, D. (2008). Incorporation of pseudouridine into mRNA yields superior

1050 nonimmunogenic vector with increased translational capacity and biological stability.
1051 *Mol Ther* 16, 1833-1840.

1052 Ke, Z., Oton, J., Qu, K., Cortese, M., Zila, V., McKeane, L., Nakane, T., Zivanov, J.,
1053 Neufeldt, C.J., Cerikan, B., *et al.* (2020). Structures and distributions of SARS-CoV-2
1054 spike proteins on intact virions. *Nature* 10.1038/s41586-020-2665-2.

1055 Keeble, A.H., Turkki, P., Stokes, S., Khairil Anuar, I.N.A., Rahikainen, R., Hytönen,
1056 V.P., and Howarth, M. (2019). Approaching infinite affinity through engineering of
1057 peptide–protein interaction. *Proceedings of the National Academy of Sciences* 116,
1058 26523-26533.

1059 Keech, C., Albert, G., Cho, I., Robertson, A., Reed, P., Neal, S., Plested, J.S., Zhu,
1060 M., Cloney-Clark, S., Zhou, H., *et al.* (2020). Phase 1-2 Trial of a SARS-CoV-2
1061 Recombinant Spike Protein Nanoparticle Vaccine. *N Engl J Med* 383, 2320-2332.

1062 Kent, S.J., Khoury, D.S., Reynaldi, A., Juno, J.A., Wheatley, A.K., Stadler, E., John
1063 Wherry, E., Triccas, J., Sasson, S.C., Cromer, D., *et al.* (2022). Disentangling the
1064 relative importance of T cell responses in COVID-19: leading actors or supporting
1065 cast? *Nat Rev Immunol* 22, 387-397.

1066 Khoury, D.S., Docken, S.S., Subbarao, K., Kent, S.J., Davenport, M.P., and Cromer,
1067 D. (2022). Predicting the efficacy of variant-modified COVID-19 vaccine boosters.
1068 medRxiv 10.1101/2022.08.25.22279237.

1069 Kleanthous, H., Silverman, J.M., Makar, K.W., Yoon, I.K., Jackson, N., and Vaughn,
1070 D.W. (2021). Scientific rationale for developing potent RBD-based vaccines targeting
1071 COVID-19. *NPJ Vaccines* 6, 128.

1072 Korber, B., Fischer, W.M., Gnanakaran, S., Yoon, H., Theiler, J., Abfalterer, W.,
1073 Hengartner, N., Giorgi, E.E., Bhattacharya, T., Foley, B., *et al.* (2020). Tracking
1074 Changes in SARS-CoV-2 Spike: Evidence that D614G Increases Infectivity of the
1075 COVID-19 Virus. *Cell* 182, 812-827.e819.

1076 Kraft, J.C., Pham, M.N., Shehata, L., Brinkkemper, M., Boyoglu-Barnum, S.,
1077 Sprouse, K.R., Walls, A.C., Cheng, S., Murphy, M., Pettie, D., *et al.* (2022). Antigen-
1078 and scaffold-specific antibody responses to protein nanoparticle immunogens. *Cell*
1079 *Rep Med* 3, 100780.

1080 Lee, H.H., Elia, N., Ghirlando, R., Lippincott-Schwartz, J., and Hurley, J.H. (2008).
1081 Midbody targeting of the ESCRT machinery by a noncanonical coiled coil in CEP55.
1082 *Science* 322, 576-580.

1083 Lu, J., Lu, G., Tan, S., Xia, J., Xiong, H., Yu, X., Qi, Q., Yu, X., Li, L., Yu, H., *et al.*
1084 (2020). A COVID-19 mRNA vaccine encoding SARS-CoV-2 virus-like particles
1085 induces a strong antiviral-like immune response in mice. *Cell Res* 30, 936-939.

1086 Madara, J.J., Han, Z., Ruthel, G., Freedman, B.D., and Harty, R.N. (2015). The
1087 multifunctional Ebola virus VP40 matrix protein is a promising therapeutic target.
1088 *Future Virol* 10, 537-546.

1089 Martins, S.A., Santos, J., Silva, R.D.M., Rosa, C., Cabo Verde, S., Correia, J.D.G.,
1090 and Melo, R. (2022). How promising are HIV-1-based virus-like particles for medical
1091 applications. *Front Cell Infect Microbiol* 12, 997875.

1092 Mastronarde, D.N. (2005). Automated electron microscope tomography using robust
1093 prediction of specimen movements. *J Struct Biol* 152, 36-51.

1094 Mastronarde, D.N., and Held, S.R. (2017). Automated tilt series alignment and
1095 tomographic reconstruction in IMOD. *J Struct Biol* 197, 102-113.

1096 McBride, C.E., Li, J., and Machamer, C.E. (2007). The cytoplasmic tail of the severe
1097 acute respiratory syndrome coronavirus spike protein contains a novel endoplasmic
1098 reticulum retrieval signal that binds COPI and promotes interaction with membrane
1099 protein. *J Virol* 81, 2418-2428.

1100 McCullough, J., Frost, A., and Sundquist, W.I. (2018). Structures, Functions, and
1101 Dynamics of ESCRT-III/Vps4 Membrane Remodeling and Fission Complexes. *Annu
1102 Rev Cell Dev Biol* 34, 85-109.

1103 Miettinen, H.M., Matter, K., Hunziker, W., Rose, J.K., and Mellman, I. (1992). Fc
1104 receptor endocytosis is controlled by a cytoplasmic domain determinant that actively
1105 prevents coated pit localization. *J Cell Biol* 116, 875-888.

1106 Miettinen, H.M., Rose, J.K., and Mellman, I. (1989). Fc receptor isoforms exhibit
1107 distinct abilities for coated pit localization as a result of cytoplasmic domain
1108 heterogeneity. *Cell* 58, 317-327.

1109 Mouquet, H., Scharf, L., Euler, Z., Liu, Y., Eden, C., Scheid, J.F., Halper-Stromberg,
1110 A., Gnanapragasam, P.N., Spencer, D.I., Seaman, M.S., *et al.* (2012). Complex-type
1111 N-glycan recognition by potent broadly neutralizing HIV antibodies. *Proc Natl Acad
1112 Sci U S A* 109, E3268-3277.

1113 Pallesen, J., Wang, N., Corbett, K.S., Wrapp, D., Kirchdoerfer, R.N., Turner, H.L.,
1114 Cottrell, C.A., Becker, M.M., Wang, L., Shi, W., *et al.* (2017). Immunogenicity and
1115 structures of a rationally designed prefusion MERS-CoV spike antigen. *Proc Natl
1116 Acad Sci U S A* 114, E7348-E7357.

1117 Pardi, N., Tuyishime, S., Muramatsu, H., Kariko, K., Mui, B.L., Tam, Y.K., Madden,
1118 T.D., Hope, M.J., and Weissman, D. (2015). Expression kinetics of nucleoside-
1119 modified mRNA delivered in lipid nanoparticles to mice by various routes. *J Control
1120 Release* 217, 345-351.

1121 Polack, F.P., Thomas, S.J., Kitchin, N., Absalon, J., Gurtman, A., Lockhart, S.,
1122 Perez, J.L., Perez Marc, G., Moreira, E.D., Zerbini, C., *et al.* (2020). Safety and
1123 Efficacy of the BNT162b2 mRNA Covid-19 Vaccine. *N Engl J Med* 383, 2603-2615.

1124 Pornillos, O., Alam, S.L., Rich, R.L., Myszka, D.G., Davis, D.R., and Sundquist, W.I.
1125 (2002). Structure and functional interactions of the Tsg101 UEV domain. *EMBO J*
1126 21, 2397-2406.

1127 Powell, A.E., Zhang, K., Sanyal, M., Tang, S., Weidenbacher, P.A., Li, S., Pham,
1128 T.D., Pak, J.E., Chiu, W., and Kim, P.S. (2021). A Single Immunization with Spike-
1129 Functionalized Ferritin Vaccines Elicits Neutralizing Antibody Responses against
1130 SARS-CoV-2 in Mice. *ACS Cent Sci* 7, 183-199.

1131 Ranieri, E., Popescu, I., and Gigante, M. (2014). CTL ELISPOT assay. *Methods Mol
1132 Biol* 1186, 75-86.

1133 Reed, L.J., and Muench, H. (1938). A Simple Method of Estimating Fifty Per Cent
1134 Endpoints. *American Journal of Epidemiology* 27, 493-497.

1135 Robbiani, D.F., Gaebler, C., Muecksch, F., Lorenzi, J.C.C., Wang, Z., Cho, A.,
1136 Agudelo, M., Barnes, C.O., Gazumyan, A., Finkin, S., *et al.* (2020). Convergent
1137 antibody responses to SARS-CoV-2 in convalescent individuals. *Nature* 584, 437-
1138 442.

1139 Rock, K.L., Reits, E., and Neefjes, J. (2016). Present Yourself! By MHC Class I and
1140 MHC Class II Molecules. *Trends Immunol* 37, 724-737.

1141 Sun, W., He, L., Zhang, H., Tian, X., Bai, Z., Sun, L., Yang, L., Jia, X., Bi, Y., Luo, T.,
1142 *et al.* (2021). The self-assembled nanoparticle-based trimeric RBD mRNA vaccine
1143 elicits robust and durable protective immunity against SARS-CoV-2 in mice. *Signal
1144 Transduct Target Ther* 6, 340.

1145 Syed, A.M., Taha, T.Y., Tabata, T., Chen, I.P., Ciling, A., Khalid, M.M., Sreekumar,
1146 B., Chen, P.Y., Hayashi, J.M., Soczek, K.M., *et al.* (2021). Rapid assessment of
1147 SARS-CoV-2-evolved variants using virus-like particles. *Science* 374, 1626-1632.

1148 van der Horst, A., Simmons, J., and Khanna, K.K. (2009). Cep55 stabilization is
1149 required for normal execution of cytokinesis. *Cell Cycle* 8, 3742-3749.

1150 van Gils, M.J., Lavell, A., van der Straten, K., Appelman, B., Bontjer, I., Poniman, M.,
1151 Burger, J.A., Oomen, M., Bouhuijs, J.H., van Vught, L.A., *et al.* (2022). Antibody
1152 responses against SARS-CoV-2 variants induced by four different SARS-CoV-2
1153 vaccines in health care workers in the Netherlands: A prospective cohort study.
1154 *PLoS Med* 19, e1003991.

1155 Votteler, J., and Sundquist, W.I. (2013). Virus budding and the ESCRT pathway. *Cell*
1156 *Host Microbe* 14, 232-241.

1157 Walls, A.C., Park, Y.J., Tortorici, M.A., Wall, A., McGuire, A.T., and Veesler, D.
1158 (2020). Structure, Function, and Antigenicity of the SARS-CoV-2 Spike Glycoprotein.
1159 *Cell* 181, 281-292 e286.

1160 Wang, Z., Muecksch, F., Cho, A., Gaebler, C., Hoffmann, H.H., Ramos, V., Zong, S.,
1161 Cipolla, M., Johnson, B., Schmidt, F., *et al.* (2022). Analysis of memory B cells
1162 identifies conserved neutralizing epitopes on the N-terminal domain of variant SARS-
1163 Cov-2 spike proteins. *Immunity* 55, 998-1012 e1018.

1164 West, A.P., Jr., Scharf, L., Horwitz, J., Klein, F., Nussenzweig, M.C., and Bjorkman,
1165 P.J. (2013). Computational analysis of anti-HIV-1 antibody neutralization panel data
1166 to identify potential functional epitope residues. *Proc Natl Acad Sci U S A* 110,
1167 10598-10603.

1168 Wu, K., Werner, A.P., Koch, M., Choi, A., Narayanan, E., Stewart-Jones, G.B.E.,
1169 Colpitts, T., Bennett, H., Boyoglu-Barnum, S., Shi, W., *et al.* (2021). Serum
1170 Neutralizing Activity Elicited by mRNA-1273 Vaccine. *N Engl J Med*
1171 10.1056/NEJMc2102179.

1172 Zakeri, B., Fierer, J.O., Celik, E., Chitcock, E.C., Schwarz-Linek, U., Moy, V.T., and
1173 Howarth, M. (2012). Peptide tag forming a rapid covalent bond to a protein, through
1174 engineering a bacterial adhesin. *Proc Natl Acad Sci U S A* 109, E690-697.

1175 Zhang, Z., Mateus, J., Coelho, C.H., Dan, J.M., Moderbacher, C.R., Galvez, R.I.,
1176 Cortes, F.H., Grifoni, A., Tarke, A., Chang, J., *et al.* (2022). Humoral and cellular
1177 immune memory to four COVID-19 vaccines. *Cell* 185, 2434-2451 e2417.

1178 Zheng, C., Shao, W., Chen, X., Zhang, B., Wang, G., and Zhang, W. (2022). Real-
1179 world effectiveness of COVID-19 vaccines: a literature review and meta-analysis. *Int*
1180 *J Infect Dis* 114, 252-260.

1181